INSTITUTE OF PHYSICAL CHEMISTRY,
POLISH ACADEMY OF SCIENCES

DOCTORAL THESIS

Hybridization Reactions in Aqueous Systems: Towards Automated Measurements

Author:
Adam Krzysztof KOWALSKI

Supervisor:
Prof. dr hab. Robert HOŁYST
Auxiliary Supervisor:
Dr. Eng. Grzegorz BUBAK

A thesis submitted in fulfillment of the requirements for the degree of Doctor of Philosophy

under

Warsaw PhD School in Natural and Biomedical Sciences at the Institute of Physical Chemistry of the Polish Academy of Sciences

Kasprzaka 44/52, 01-224 Warsaw, Poland

Warsaw, May 2025

Podziękowania

Nie doszedłbym tak daleko w swojej ścieżce kariery naukowej, gdyby nie pomoc kilku szczególnych dla mnie osób. Dlatego na wstępie chciałbym serdecznie podziękować:

moim **Rodzicom**, którzy od samego początku byli przy mnie, wspierali mnie w każdej decyzji i nieustannie pomagali w realizacji moich planów.

mojej **Żonie, Wiktorii**, która zawsze potrafi mnie rozbawić, dodać energii do działania, a także ostudzić moje czasem zbyt optymistyczne pomysły.

prof. Robertowi Hołystowi, bez którego ten doktorat nigdy by nie powstał. Dziękuję za wszystkie dobre rady, szanse, które mi umożliwiłeś, oraz za to, że zawsze mogłem przyjść i zwyczajnie porozmawiać.

Patrycji Kuźmie, która nigdy nie pozwoli skrzywdzić swoich "dzieci". Dziękuję za każde Twoje dobre słowo, za to, że nigdy nie odmawiałaś pomocy i sprawiałaś, że wszelkie formalności w instytucie stawały się błahostką.

Grzegorzowi Bubakowi i Krzysztofowi Bielcowi, których zawsze mogłem poprosić o radę i którzy nauczyli mnie, jak poruszać się w świecie nauki.

Tomkowi Pirosowi i Antoniemu Lisowi – za pomoc w realizacji badań i nietypowe poczucie humoru. Bez Was ten doktorat nie byłby taki sam.

Wszystkim moim Przyjaciołom i członkom zespołu 10 – za wspólny czas, rozmowy i wsparcie.

This work was supported by the National Science Centre within the grants ***Preludium Bis 2*** *no. 2020/39/O/ST4/00877 and* ***Preludium 22*** *no. 2023/49/N/ST4/01008.*

Publications

Google Scholar
ORCID, 0000-0003-0172-2622

1. **Kowalski, A.K.**; Bielec, K.; Bubak, G.; Żuk, P.J.; Czajkowski M.; Sashuk V.; Huck W.T.S.; Hołyst, R. "Effective screening of Coulomb repulsions in water accelerates reactions of like-charged compounds by orders of magnitude" *Nature Communications* 2022, 13, 6451.

2. Bielec, K.; **Kowalski, A.K.**; Bubak, G.; Witkowska Nery E.; Hołyst R. "Ion Complexation Explains Orders of Magnitude Changes in the Equilibrium Constant of Biochemical Reactions in Buffers Crowded by Non-ionic Compounds" *The Journal of Physical Chemistry Letters* 2022, 13, 1, 112-117.

3. **Kowalski A.K.**; Piros T.; Blonski S.; Kurniawan T.; Korczyk P.M.; Hołyst R. "Microfluidic-based Platform for the semi-Automated Measurement of Concentration, Diffusion Coefficient, and Equilibrium Constant of Biomolecules, *submitted*."

4. **Kowalski A.K.**; Lis A.; Piros T.; Bielec K.; Bubak G.; Bernatowicz P.; Hołyst R. "Molecular Crowding: Quantifying the Interplay Between Depletion Interactions, Crowding-Induced Destabilization Effects and Electrostatics, *submitted*."

5. Bubak G.; Lis A.; Kolankowski K., **Kowalski A.K.**; Mamot A.; Perzanowska O.; Bielec K.; Kowalska J.; Burdzy K.; Jemielity J.; Hołyst R. "Quantification of mRNA and Oligonucleotide Export Kinetics Reveal a Low Effective Availability of Nuclear Pores in Living Human Cells, *submitted*."

Publications 1, 2, 3, and 4 are part of this dissertation.

Abstract

Hybridization reactions, which involve the specific pairing of complementary nucleic acid strands, are fundamental to various biological processes and biomedical applications. In an aqueous environment, these reactions are particularly significant due to the intrinsic solubility and stability of nucleic acids in water-based solutions.[1] The selective hybridization of nucleic acid sequences underlies a wide array of techniques, including DNA microarray technology, fluorescence *in situ* hybridization (FISH), biosensors, and therapeutic oligonucleotides.[2–5] For instance, DNA microarrays utilize the hybridization of fluorescently labeled cDNA to immobilize probes, enabling high-throughput gene expression analysis.[6] FISH enables the spatial visualization and quantitation of specific DNA and mRNA sequences within cells, facilitating studies of chromosomal abnormalities such as aneuploidy and the spatial organization of centromeres.[7] In therapeutics, antisense oligonucleotides and small interfering RNAs (siRNAs) employ hybridization to silence target genes, offering promising strategies for treating genetic disorders and viral infections.[8]

Despite their broad utility, hybridization reactions are sensitive to environmental conditions, particularly in aqueous solutions. Factors such as pH, temperature, ionic strength, and molecular crowding influence the kinetics and thermodynamics of hybridization. High ionic strength stabilizes duplex formation by shielding electrostatic repulsion between negatively charged phosphate backbones, whereas extreme pH can disrupt hydrogen bonding and base pairing.[9, 10] Moreover, macromolecular crowding modulates hybridization equilibria by introducing steric hindrance, thereby altering association, dissociation, and equilibrium constants.[11, 12] At low crowder concentrations ($<$15 wt.%), the equilibrium constant K of DNA-DNA complex formation increases by an order of magnitude,[13] whereas at higher concentrations, K decreases even up to three orders of magnitude.[14] These unintuitive changes are controlled by two counteracting effects: depletion forces and crowding-induced destabilization, whereas electrostatics adds another layer

of complexity to the system. Despite extensive studies, to this date, no physical model fully explains the interplay of these phenomena.

The first and second sections of this thesis investigate the influence of ions and oppositely charged molecules on nucleic acid association rates, as well as the impact of molecular crowding and ions on DNA-DNA interactions at equilibrium. The results combine experimental data with theoretical models. The first model predicts association rates of like-charged reactants in the presence of oppositely charged catalyst molecules in aqueous solutions. The second model elucidates the role of molecular crowding in modulating DNA-DNA hybridization and the interplay between electrostatics, depletion interactions, and crowding-induced destabilization.

To study DNA-DNA interactions at equilibrium, Förster Resonance Energy Transfer (FRET) and Molecular Brightness Analysis (MBA) are employed. These techniques allow the monitoring of equilibrium shifts in response to variations in pH, ionic strength, molecular crowding, and ion concentration.[14–20] When integrated with Fluorescence Correlation Spectroscopy (FCS), they provide single-molecule resolution within femtoliter volumes. FRET offers superior accuracy due to its high signal-to-noise ratio, but it requires dual fluorescent labeling and precise positioning of dyes within 1–10 nm of interacting molecules. In contrast, MBA, with a lower signal-to-noise ratio, simplifies experimental design by eliminating the need for site-specific fluorescent labeling. However, both methods are laborious and have inherent limitations in throughput.

Determining K for a simple $A + B \rightleftharpoons AB$ reaction requires extensive dilution series, typically involving 20–30 different concentration ratios.[21] Given the sample preparation and measurement requirements, such experiments are time-consuming, often taking several hours. Large-scale studies, such as those examining pH or ionic strength dependencies, further amplify the experimental burden, as the number of required samples increases by an order of magnitude. Reducing the number of data points per K determination is undesirable, as it increases measurement error from approximately 15% (with 30 samples) to $\sim$60% (with 10 samples). Additionally, the standard protocol typically relies on disposable well plates, which accommodate 200 µL of solution per well, leading to substantial material consumption and high costs.

Even after sample preparation, manual plate exchange is required, depending on the number of wells in the plate, further impeding efficiency.

To address these limitations, the third section of this thesis presents a microfluidic-based platform that automates both sample handling and measurement. This system streamlines experimental workflows, significantly reducing manual labor by requiring only an initial setup and microscope calibration. Once initiated, the platform operates with minimal user intervention, decreasing the total time required for K determination from approximately 180 minutes to 35 minutes. Moreover, it enhances the accuracy of MBA while reducing reagent consumption by three orders of magnitude, from $\sim$200 µL per sample in conventional protocols to $\sim$100 nL per droplet in the microfluidic system. These improvements enhance both the efficiency and cost-effectiveness of DNA hybridization studies, facilitating large-scale investigations of nucleic acid interactions under various conditions.

Streszczenie

Reakcje hybrydyzacji, polegające na specyficznym łączeniu komplementarnych nici kwasów nukleinowych, odgrywają kluczową rolę zarówno w procesach biologicznych, jak i w licznych zastosowaniach biotechnologicznych. W środowisku wodnym ich znaczenie dodatkowo wzrasta – kwasy nukleinowe cechują się wysoką rozpuszczalnością i stabilnością w roztworach wodnych.[1] Selektywność tych oddziaływań stanowi fundament wielu nowoczesnych metod, takich jak mikromacierze DNA, fluorescencyjna hybrydyzacja *in situ* (FISH), biosensory czy terapie z zastosowaniem oligonukleotydów.[2–5] Przykładowo, mikromacierze wykorzystują fluorescencyjnie znakowane cząsteczki cDNA, które hybrydyzują z sondami osadzonymi na powierzchni, umożliwiając jednoczesną analizę ekspresji tysięcy genów.[6] Z kolei metoda FISH pozwala na lokalizację konkretnych sekwencji DNA lub mRNA w komórkach, co znajduje zastosowanie m.in. w diagnostyce aberracji chromosomowych, takich jak aneuploidie, oraz w badaniach organizacji przestrzennej centromerów.[7] Dodatkowo, w terapii genowej wykorzystuje się oligonukleotydy antysensowne oraz interferujące RNA (siRNA), które poprzez hybrydyzację wyciszają określone geny, oferując nowe możliwości leczenia chorób genetycznych i zakaźnych.[8]

Pomimo szerokiego zastosowania, skuteczność reakcji hybrydyzacji jest silnie uzależniona od warunków środowiskowych, zwłaszcza w roztworach wodnych. Parametry takie jak pH, temperatura, siła jonowa i zatłoczenie molekularne wpływają na szybkość i wydajność tworzenia dupleksów. Wysoka siła jonowa sprzyja hybrydyzacji, ponieważ jony dodatnie neutralizują odpychanie elektrostatyczne pomiędzy ujemnie naładowanymi nićmi DNA. Z kolei skrajne wartości pH mogą zakłócać tworzenie wiązań wodorowych i prawidłowe parowanie zasad.[9, 10] Zatłoczenie molekularne dodatkowo zmienia przebieg reakcji – ogranicza dostępność przestrzeni, co prowadzi do zmian w szybkościach asocjacji i dysocjacji oraz wartości stałych równowagi reakcji.[11, 12] Przy niskich stężeniach cząsteczek powodujących zatłoczenie (poniżej 15 % wagowych), obserwuje się wzrost stałej równowagi hybrydyzacji kwasów nukleinowych K nawet o rząd wielkości,[13] natomiast

przy wyższych stężeniach, spadek K sięgający trzech rzędów wielkości.[14] Ten nietypowy efekt wynika z działania przeciwstawnych sił: satbilizujących sił wyczerpania (depletion) oraz szeroko pojętej destabilizacji struktury dupleksu przez zatłoczenie. Dodatkowym czynnikiem komplikującym zrozumienie wpływu zatłoczonego środowiska na reakcje kwasów nukleinowych są oddziaływania elektrostatyczne.

Dotychczas nie został opracowany jednen spójny model, który w pełni wyjaśniałby współdziałanie tych zjawisk. W dwóch pierwszych częściach tej pracy przedstawiono wpływ jonów i przeciwnie naładowanych cząsteczek na szybkość asocjacji DNA-DNA, a także efekt zatłoczenia i siły jonowej na stan równowagi reakcji hybrydyzacji. Na podstawie wyników eksperymentalnych opracowano modele teoretyczne. Pierwszy z nich opisuje przyspieszenie reakcji pomiędzy jednoimiennie naładowanymi cząsteczkami w obecności przeciwnie naładowanych katalizatorów w środowisku wodnym. Z kolei, drugi model analizuje wpływ zatłoczenia molekularnego na równowagę hybrydyzacji DNA, uwzględniając współdziałanie sił wyczerpania, oddziaływań elektrostatycznych i destabilizacji wynikającej z ograniczeń przestrzennych.

W badaniach hybrydyzacji DNA-DNA zastosowano techniki Transferu Energii Rezonansu Förstera (FRET) oraz Analizę Jasności Molekularnej (MBA). Obie te metody pozwalają śledzić przesunięcia równowagi w odpowiedzi na zmiany pH, siły jonowej, zatłoczenia oraz stężenia jonów.[14–20] Natomiast, w połączeniu z Spektroskopią Korelacji Fluorescencji (FCS) umożliwiają pomiary z rozdzielczością pojedynczych cząsteczek w objętościach rzędu femtolitrów. Technika FRET charakteryzuje się wysoką dokładnością i korzystnym stosunkiem sygnału do szumu, jednak wymaga znakowania cząsteczek dwoma barwnikami fluorescencyjnymi oraz ich precyzyjnego rozmieszczenia w odległości 1–10 nm. MBA, mimo niższego stosunku sygnału do szumu, upraszcza procedurę – funkcjonuje przy użyciu jednego barwnika fluorescencyjnego. Obie metody mają jednak ograniczenia pod względem przepustowości.

Wyznaczenie stałej równowagi K dla reakcji $A + B \rightleftharpoons AB$ wymaga wykonania serii rozcieńczeń, obejmującej zazwyczaj 20–30 różnych stosunków stężeń reagentów.[21] Przygotowanie próbek oraz same pomiary są

czasochłonne i mogą trwać wiele godzin. W badaniach zależnych od pH lub siły jonowej, liczba wymaganych próbek może wzrosnąć nawet kilkadziesiąt razy. Ograniczenie liczby punktów pomiarowych powoduje istotny wzrost błędu – z około 15 % (dla 30 punktów) do nawet 60 % (dla 10 punktów). Dodatkowo, standardowe procedury wykorzystują jednorazowe płytki wielodołkowe mieszczące najczęściej 200 µL roztworu w każdym dołku, co prowadzi do dużego zużycia materiałów i wysokich kosztów. Nawet po przygotowaniu próbek konieczna jest ręczna wymiana płytki co kilka pomiarów w zależności od liczby dołków w płytce, co dodatkowo ogranicza wydajność.

Aby sprostać tym ograniczeniom, w trzeciej części pracy zaprezentowano platformę mikroprzepływową, która automatyzuje zarówno przygotowanie próbek, jak i pomiar. System ten znacząco upraszcza przebieg eksperymentów, ograniczając udział użytkownika do konfiguracji początkowej i kalibracji mikroskopu. Po uruchomieniu platforma działa autonomicznie, skracając czas potrzebny na wyznaczenie K z około 180 minut do 35 minut. Układ dodatkowo poprawia dokładność pomiarów MBA i redukuje zużycie odczynników o trzy rzędy wielkości – z około 200 µL w standardowej procedurze do około 100 nL na próbkę w układzie mikroprzepływowym. Dzięki tym usprawnieniom badania hybrydyzacji DNA stają się bardziej
wydajne, oszczędne i lepiej przystosowane do analiz wysokoprzepustowych w różnych warunkach środowiskowych.

Contents

Chapter 1

Introduction

This section is divided into six paragraphs. The first one covers nucleic acid applications, structure, and interactions, while the second one introduces molecular crowding and its implications for biomolecule interactions. Further, the thesis describes physical chemistry principles, allowing for the determination of the strength of nucleic acid interactions at equilibrium and their association rates. The phenomenon of fluorescence is then introduced as a fundamental tool for monitoring DNA-DNA hybridization, with a focus on fluorescence-based techniques employed in this study. Finally, the concept of microfluidics is presented as a lab-on-a-chip approach aimed at enhancing measurement throughput and minimizing reagent consumption.

1.1 Nucleic Acids

1.1.1 Nucleic Acids: Functions and Applications

Nucleic acids, classified as biopolymers, are fundamental to life. The two main types, deoxyribonucleic acid (DNA) and ribonucleic acid (RNA) are composed of nucleotide monomers that form long chains called polynucleotides. These molecules play a critical role in storing, transmitting, and utilizing genetic information.

DNA serves as the genetic blueprint, encoding hereditary information in the precise sequence of its nucleotides. This blueprint is replicated during cell division to ensure that each daughter cell inherits an identical copy. Replication begins at specific regions called origins, where the double helix unwinds to form replication forks. Here, DNA polymerase, the central enzyme in this

process, synthesizes new strands by adding complementary nucleotides to the parental template while proofreading to minimize errors.

The genome, comprising the complete set of an organism's genetic material, provides the instructions for cellular processes through gene expression. This process is mediated by two interconnected mechanisms: transcription and translation, with transcription and certain aspects of translation (e.g., codon–anticodon pairing) relying on nucleic acid hybridization. Transcription uses DNA as a template to synthesize RNA in three stages: initiation, where RNA polymerase binds to the promoter region; elongation, during which the RNA strand is extended; and termination, marking the release of the RNA molecule. While some RNA molecules function directly, most serve as intermediates in protein synthesis.

Protein synthesis, the second step in gene expression, involves translation, where the nucleotide sequence of RNA is converted into a chain of amino acids to form proteins. Like transcription, translation occurs in three stages: initiation, elongation, and termination. This flow of genetic information – from DNA to RNA to proteins – is a basis of molecular biology and ensures the proper functioning of cells. Figure 1.1 illustrates these coordinated processes.

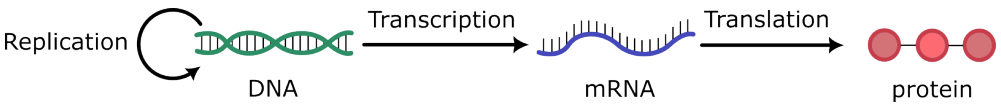

FIGURE 1.1: Diagram of intracellular processes utilizing hybridization reactions: replication, transcription, and translation.

In addition to their genetic roles, nucleic acids are vital in research, medicine, and biotechnology. Their ability to form specific complementary pairs, a process known as hybridization, is the foundation for many applications. Key strategies include:

- **CRISPR–Cas system**. The CRISPR–Cas system represents a revolutionary tool in genetic engineering, renowned for its selectivity in targeting and modifying genetic material. Derived from a natural defense mechanism found in bacteria and archaea, this system uses a guide RNA to direct the Cas protein, typically Cas9, to specific DNA sequences. Upon binding to the target sequence, the Cas protein induces double-strand

breaks, which can be repaired through either non-homologous end joining or homology-directed repair. These repair pathways allow precise editing of genes, including inserting, deleting, or replacing DNA sequences.[22, 23]

- **Antisense oligonucleotides (ASOs)**. ASOs are short, single-stranded nucleic acids binding specifically to complementary DNA or RNA sequences. This binding inhibits processes such as replication, transcription, or translation. They are used to identify and validate target proteins and as therapeutic tools. Current research explores their potential for treating cancer, autoimmune diseases, neurological disorders, viral infections, and other conditions.[24, 25]

- **Aptamers**. Aptamers are single-stranded oligonucleotides that specifically bind to target molecules, including nucleotides, proteins, peptides, and chemical compounds. Their high specificity and adaptability make them valuable in diagnostics and therapeutics. Aptamers are widely used in biosensors for detecting environmental contaminants, such as heavy metals (e.g., Pb^{2+}, Hg^{2+}) or toxic substances (e.g., pesticides, mycotoxins).[26] They also facilitate drug delivery by transporting therapeutic agents into cells.[27]

- **Antigene strategies**. Antigene approaches aim to repair genomic mutations or regulate disease-associated genes. They utilize oligonucleotides that interact with DNA or RNA to form triple helix structures (triplexes), which can inhibit processes such as transcription or replication.[28] These strategies are also useful for studying nucleic acid interactions with proteins and enzymes in defining the DNA and RNA topology.[29]

- **RNA interference (RNAi)**. RNA interference is a natural gene-silencing process mediated by small noncoding RNA molecules, such as small interfering RNAs (siRNAs) and microRNAs (miRNAs). RNAi degrades complementary mRNA, preventing gene expression. This mechanism

has significant potential for developing therapies, with promising applications in treating cancer, autoimmune diseases, and genetic disorders.[30]

1.1.2 Nucleic Acids: Structure and Interactions

Nucleic acids are composed of nucleotides, which consist of a sugar residue, a nitrogenous base, and a phosphate group. The type of sugar determines the classification of nucleic acids. RNA contains D-ribose, which has a hydroxyl group (-OH) at position 2, while DNA contains 2-deoxy-D-ribose, where the hydroxyl group is replaced by a hydrogen atom (Figure 1.2). This distinction influences the properties and functions of RNA and DNA.

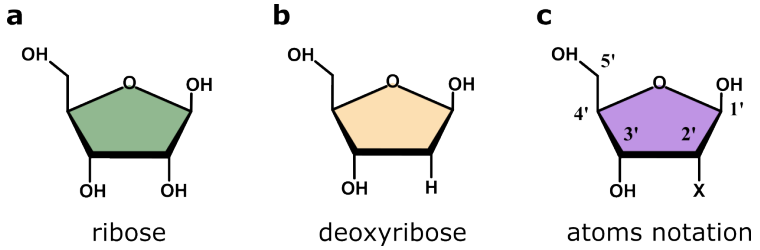

FIGURE 1.2: Sugar residues of **(a)** RNA, **(b)** DNA, and **(c)** their notation.

Nitrogenous bases, which are attached to the sugar residue, are aromatic rings categorized as purines: adenine [A] and guanine [G] or pyrimidines: cytosine [C], thymine [T], and uracil [U] (Figure 1.3). Thymine is unique to DNA, while uracil is exclusive to RNA. Thymine differs from uracil by adding a methyl group at position 5. RNA also contains modified nitrogenous bases, such as ribothymine, thiouracil, dihydrouracil, pseudouracil, and inosine, which enhance its structural and functional diversity.

The nitrogenous base forms a nucleoside when it attaches to the sugar at position 1′ via an N-glycosidic bond. When a phosphate group is added to the nucleoside at the 5′ carbon, a nucleotide is formed. Nucleotides such as ATP (adenosine-5′-triphosphate), GDP (guanosine-5′-diphosphate), and dTMP (deoxythymidine-5′-monophosphate) serve not only as building blocks for nucleic acids but also as energy carriers and components of coenzymes,

including NAD (nicotinamide adenine dinucleotide), FAD (flavin adenine dinucleotide), and coenzyme A.[31–33]

In nucleic acids, nucleotides are linked by 3′,5′-phosphodiester bonds, connecting the 3′ carbon of one sugar to the 5′ carbon of another via a phosphate group. This linkage forms the sugar-phosphate backbone, with one end of the chain bearing a free phosphate group (the 5′ end) and the other end carrying a free hydroxyl group (the 3′ end). The nucleotide sequence is typically written from the 5′ to the 3′ end, as in 5′-ATA CGC-3′, or simply ATA CGC. This sequence notation is critical because reversing the sequence (e.g., CGC ATA) represents a different oligonucleotide with distinct properties.

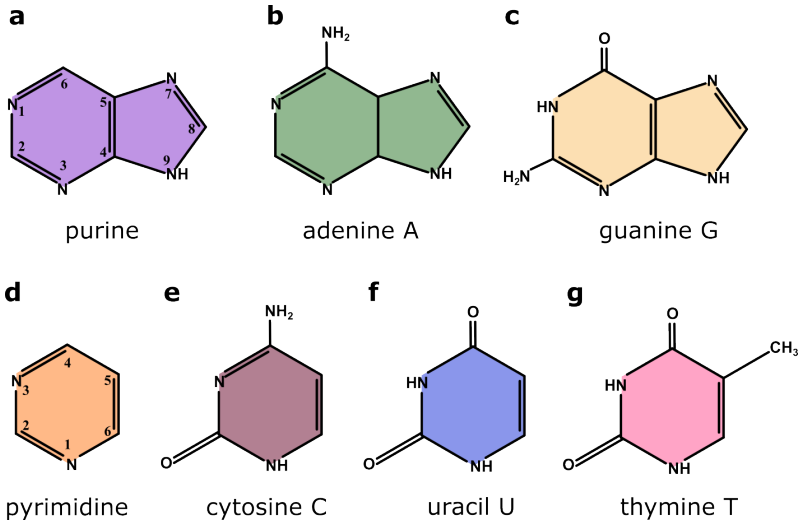

FIGURE 1.3: Nitrogenous bases of DNA and RNA nucleotides divided into **(a)** purines: **(b)** adenine and **(c)** guanine, and **(d)** pyrimidines: **(e)** cytosine, **(f)** uracil, and **(g)** thymine. Thymine is specific to DNA, and uracil is specific to RNA.

DNA molecules adopt a double helix structure, comprising two antiparallel polynucleotide strands coiled around a common axis. This structure is stabilized by hydrogen bonds between complementary nitrogenous bases: adenine pairs with thymine (A-T) via two hydrogen bonds, and cytosine pairs with guanine (C-G) via three hydrogen bonds (Figure 1.4). The sequence of one strand dictates the complementary sequence of the other, enabling precise replication and information transfer. Additional stabilization arises from π-π stacking interactions between the planar aromatic rings of nitrogenous bases

and hydrophobic interactions, which expel water molecules from the helical interior. These interactions contribute to the unique structural integrity of the DNA double helix.

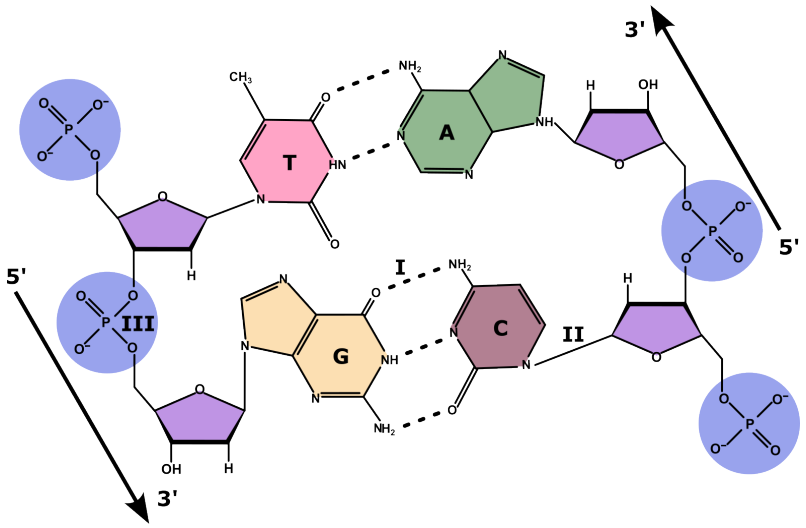

FIGURE 1.4: DNA backbone with specific bonds: **(I)** hydrogen bond, **(II)** N-glycosidic bond, and **(III)** 3′,5′-phosphodiester bond. A, T, G, and C represent adenine, thymine, guanine, and cytosine, respectively.

DNA demonstrates remarkable conformational variability. Under physiological conditions, the B-DNA form, a right-handed helix with 10.5 base pairs per turn, predominates. Other helical forms include A-DNA, observed under dehydrating conditions, and Z-DNA, a left-handed helix favored by high ionic strength.[34] Non-canonical structures, such as triplexes and G-quadruplexes, can also form and be stabilized by non-Watson-Crick base pairing or base stacking.[35]

Unlike DNA, RNA primarily exists as a single-stranded molecule. However, intramolecular base pairing allows it to form secondary structures such as stem loops, bulges, and hairpins. These regions often adopt an A-form helix and contribute to RNA's functional versatility. RNA can further fold into complex tertiary structures, enabling diverse biological roles.

The structure and function of nucleic acids are intricately governed by a

delicate balance of interactions, including base pairing, stacking, and associations with proteins and small molecules. Central to these processes are electrostatic interactions, driven by the polyanionic nature of the sugar-phosphate backbone, which carries negatively charged phosphate groups. This intrinsic charge facilitates interactions with water molecules, organic ions, and metal cations, contributing significantly to the stability and folding of nucleic acid structures. The surrounding ionic environment further modulates these interactions through ionic screening, which is quantified by the Debye length (λ_D). It is defined as:

$$\lambda_D = \left(\frac{\varepsilon_0 \varepsilon k_B T}{e^2 \sum_i n_i z_i^2} \right)^{1/2}, \tag{1.1}$$

where ε_0 is the vacuum permittivity, ε is the relative permittivity of the medium, k_B is the Boltzmann constant, T is the absolute temperature, e is the elementary charge, n_i is the number density of ionic species i, and z_i is the charge number of each ion. The Debye length determines the effective range of electrostatic interactions, with higher ionic concentrations leading to shorter λ_D, thus enhancing charge screening and influencing nucleic acid folding and stability.

In vivo, nucleic acids function within a highly crowded intracellular milieu, where elevated concentrations of macromolecules such as proteins and metabolites create a complex biophysical environment. This molecular crowding not only restricts the available volume but also promotes the formation of compact secondary and tertiary nucleic acid structures.[36, 37] Additionally, crowding enhances interactions with ligands and proteins, often leading to altered binding affinities and conformational dynamics.[38]

1.2 Biomolecule Interactions in Crowded Environments

A crowded environment, from the perspective of molecules, refers to a system where macromolecules such as proteins, nucleic acids, metabolites, and polysaccharides occupy 30–40% of the available volume.[39, 40] This complex milieu profoundly influences biomolecular interactions and cellular functions, challenging the interpretation of biochemical processes studied in vitro.[41, 42] Crowded environments alter the physical properties of the

intracellular space, including viscosity and diffusion, thereby affecting the movement and interaction rates of biomolecules. Furthermore, extreme crowding conditions may lead to protein aggregation or misfolding due to restricted conformational freedom, while entropic forces can promote complex formation of biomolecules.[43, 44]. These phenomena highlight a delicate balance between stabilizing and destabilizing effects in such systems.

The consequences of molecular crowding are primarily governed by two key mechanisms: depletion forces and crowding-induced destabilization. Depletion forces dominate at lower crowder concentrations (<15 wt.%) and arise because crowding agents cannot access the narrow space between closely positioned biomolecules. This results in a net osmotic pressure difference that drives macromolecules together to minimize excluded volume.[45] As a result, the excluded volumes surrounding the reactants overlap, increasing the total volume accessible to crowders (Figure 1.5). Such effects can promote biomolecular association and stabilize complex structures, i.e., folded proteins and hybridized DNA strands.[46, 47] For instance, the presence of crowding agents like polyethylene glycols (PEG) or polysaccharides has been shown to enhance protein folding and functional stability by favoring compact conformations with minimal excluded volume.[45, 48, 49]

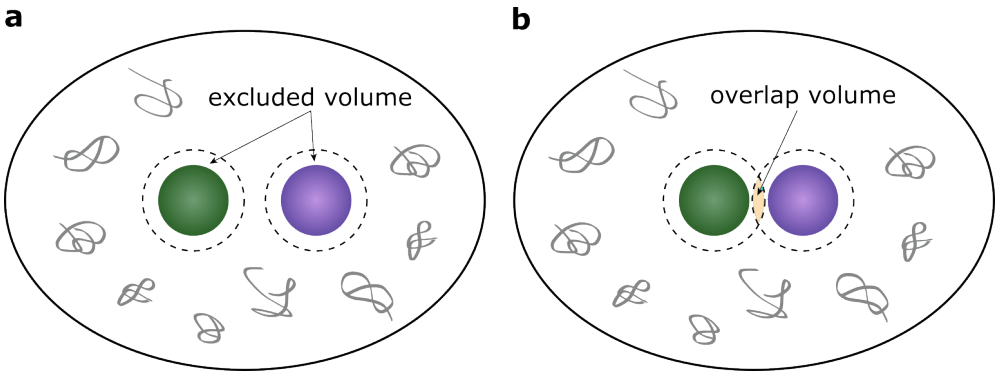

FIGURE 1.5: As a result of depletion interactions, **(a)** the excluded volume around reactants **(b)** overlaps (yellow area), thereby increasing the total volume available for molecular crowders (grey coils).

At higher crowder concentrations (>15 wt.%), crowding-induced destabilization effects become a dominant factor.[50] These include increased viscosity, steric hindrance, alteration of hydrophobic forces and solvent properties, induction of conformational changes, liquid-liquid phase separation, and direct crowder-reactant interactions. The increased viscosity in such environments slows the diffusion of reactants, shifting the reactions into a diffusion-limited regime.[49] At the same time, spatial constraints imposed by crowders hinder the proper alignment of reactants, lowering association rates and introducing unfavorable interactions.[41] These restrictions reduce the effective volume available for reactants to associate, introducing entropic penalties that counteract the stabilizing effects of depletion forces.[51] Additionally, crowding perturbs the properties of the solvent by decreasing the water activity and lowering the dielectric constant, which can alter the solubility of the reactants and shift the reaction equilibria.[52]

Electrostatics introduces another layer of complexity to the dynamics of molecular crowding. In crowded conditions, the close proximity of charged macromolecules amplifies electrostatic forces, as the reduced dielectric constant of the dense medium limits charge screening. This intensifies long-range interactions, which can promote or inhibit specific associations depending on the nature of the charges involved. For example, electrostatic attraction can enhance the assembly of oppositely charged biomolecules, such as protein-DNA complexes, while repulsion between similarly charged molecules may inhibit their association.[53] Crowded environments also affect ion distribution, as confined regions can concentrate or exclude certain ionic species, altering local ionic strength.[54] For instance, crowding agents like PEGs or polysaccharides can bind cations, such as Na^+, further modulating interaction dynamics.[14] Electrostatic forces can also synergize with depletion forces to stabilize compact macromolecular conformations, such as folded proteins or nucleic acid structures. However, in extreme crowding conditions, the combination of steric hindrance and strong electrostatic repulsion may promote aggregation or misfolding, particularly in highly charged biomolecules.[42]

Understanding the dual nature of molecular crowding across the full spectrum of concentrations is essential for accurately replicating intracellular conditions in vitro and designing experiments that reflect the true behavior of

biomolecules. Crowding has far-reaching implications in areas such as drug discovery, diagnostics, and the development of artificial cells. For example, incorporating crowding effects into diagnostic assays can improve their physiological relevance and reliability by mimicking the binding dynamics of biomolecules in vivo.[55] Similarly, therapeutic strategies that account for crowding-induced stabilization or inhibition of targets can lead to more effective drug design.[56]

1.3 Determining the Strength of Interactions and Reaction Rate

1.3.1 Equilibrium Constant

Chemical reactions transform substrates into products. These reactions can be classified as irreversible, progressing in one direction until the substrates are consumed ($A + B \rightarrow C$), or reversible, occurring in both directions ($A + B \leftrightharpoons AB$). Under favorable conditions, reversible reactions reach a state where the forward and reverse reaction rates are equal. This dynamic balance is known as equilibrium.[57]

At equilibrium, the concentrations of reactants and products remain constant, with no observable macroscopic changes. The temperature distribution throughout the system is uniform, and the Gibbs free energy of the system reaches a minimum at constant temperature and pressure. From an external perspective, the system appears stationary, with no macroscopic changes. However, on the molecular level, processes such as chemical reactions may still occur in both directions at equal rates. In a closed system, thermal, mechanical, and chemical equilibrium are maintained, with no net transfer of heat, work, or matter.[58]

The parameter characterizing these equilibrium processes is the equilibrium constant K, which is defined as the ratio of the products to reactants at equilibrium. For the reaction $aA + bB \leftrightharpoons cAB$, K is expressed as:

$$K = \frac{[\mathrm{AB}]_{\mathrm{eq}}^{c}}{[\mathrm{A}]_{\mathrm{eq}}^{a}[\mathrm{B}]_{\mathrm{eq}}^{b}}, \tag{1.2}$$

where the square brackets denote molar concentrations, *eq* indicates equilibrium conditions, and a, b, and c are the stoichiometric coefficients of the reaction.

The equilibrium constant is not just a mathematical construct but has thermodynamic significance. It is linked to the standard Gibbs free energy change ΔG°:

$$\Delta G^\circ = -RT \ln K, \tag{1.3}$$

where R is the universal gas constant, and T is the absolute temperature. A negative ΔG° indicates a reaction favoring product formation, while a positive ΔG° implies that reactants are favored.

The equilibrium constant depends on external factors such as temperature. For endothermic reactions, higher temperatures increase K, favoring product formation. Conversely, exothermic reactions exhibit a decrease in K with rising temperatures. Le Chatelier's principle further explains how a system at equilibrium responds to changes in concentration, pressure, or temperature to minimize the disturbance.

The equilibrium constant has practical importance, allowing chemists to optimize reaction conditions and estimate the stability of products. For nucleic acids, K helps assess interaction strength and product stability.[59]

1.3.2 Reaction Kinetics

Thermodynamics determines whether a reaction is energetically favorable and defines the equilibrium state, but it does not provide information about how fast the reaction proceeds. Time is not a factor in thermodynamic descriptions, and the duration required to reach equilibrium is governed by kinetic parameters rather than whether a reaction is exothermic or endothermic. Furthermore, stoichiometry alone does not reveal the reaction mechanism. Thus, the kinetics of each reaction must be independently determined, often using advanced techniques like fluorescence measurements to analyze molecular interactions.[60]

In reversible reactions, the classification of species as reactants or products is arbitrary and depends on the direction from which the reaction is approached. Whether the system is initiated with c moles of AB or with a moles

of A and b moles of B, it will evolve toward an equilibrium state defined by the equilibrium constant, as illustrated in Figure 1.6.

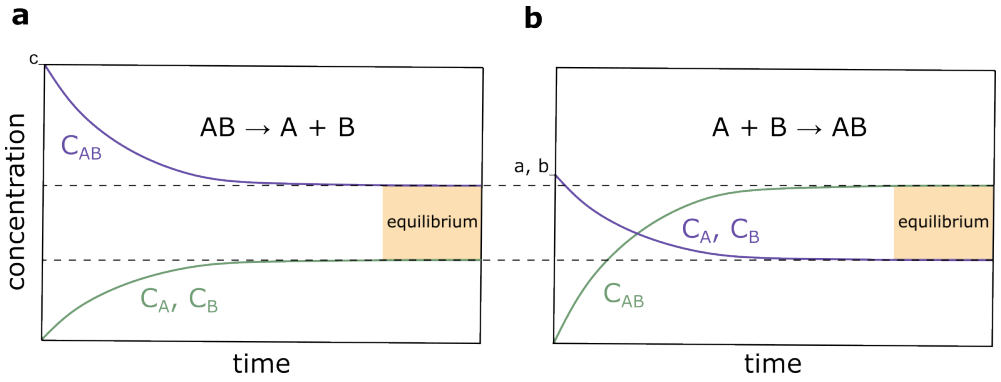

FIGURE 1.6: Change in reagent concentrations in relation to reaction time. **(a)** Dissociation of molecule AB, **(b)** Formation of molecule AB. The direction of the reversible reaction is relative and depends on the initial concentrations of the reactants. a, b, and c are the initial concentrations of A, B, and AB, respectively.

Reactions proceed at varying rates. Some may reach equilibrium within milliseconds, while others take days.[61] The reaction rate v depends on the nature and strength of bonds between reactants. Acid-base and ionic reactions are typically rapid, whereas covalent bond formation, such as rusting, occurs much more slowly.[62]

The physical state of reactants also influences v. In a single phase (e.g., liquids), molecules mix freely, allowing rapid contact. In contrast, reactions involving different phases are limited to the interface area. Increasing the surface area or using catalysts can enhance reaction rates. Other factors include temperature, reactant concentrations, and the presence of inhibitors.[63]

Unlike the equilibrium constant, v depends on the concentrations of reactants and products. The rate of a reaction is mathematically expressed as the change in substrate S or product P concentration over time t:

$$v = -\frac{\Delta[S]}{\Delta t} \quad \text{or} \quad v = \frac{\Delta[P]}{\Delta t}. \tag{1.4}$$

Since substrate concentrations decrease over time, rates based on them are preceded by a negative sign.

For nucleic acid hybridization illustrated in Figure 1.7, the reaction rate is given by:

$$v = k_+[A]^\alpha[B]^\beta - k_-[AB]^\gamma, \tag{1.5}$$

where k_+ and k_- are rate constants for the forward and reverse reactions, respectively. The terms α, β, and γ represent the partial reaction orders for the reactants and product, respectively, while the sum of these coefficients defines the overall reaction order.

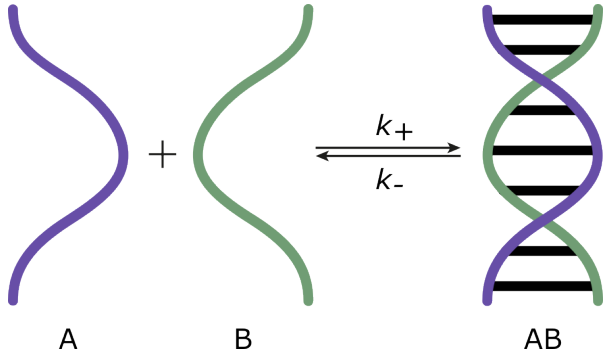

FIGURE 1.7: The association of complementary single-stranded DNA molecules, A and B, into a double-stranded complex AB. The reaction proceeds with a forward rate constant k_+ representing hybridization and a backward rate constant k_- corresponding to strand dissociation.

At equilibrium, the forward and reverse reaction rates are equal:

$$k_+[A][B] = k_-[AB], \tag{1.6}$$

which for an elementary bimolecular reaction leads to:

$$K = \frac{[AB]}{[A][B]} = \frac{k_+}{k_-}. \tag{1.7}$$

This relationship holds under the assumption that the reaction proceeds through a single elementary step and that activities can be approximated by concentrations.

Nucleic acid hybridization is frequently modeled as an elementary bimolecular association reaction, particularly under dilute conditions and in the

absence of significant secondary structure formation. Under these assumptions, the association rate is given by:

$$v = k_+[A][B]. \tag{1.8}$$

When the initial concentrations of the two strands are equal, the rate simplifies to:

$$v = k_+[A]^2. \tag{1.9}$$

This expression is valid when the reverse reaction is negligible, e.g., at early time points or under conditions where hybridization is strongly favored.

From Equation 1.4, the reaction rate can be determined by calculating the change in substrate concentration as a function of time. This allows Equation 1.9 to be expressed in terms of a derivative:

$$-\frac{d[A]}{dt} = k_+[A]^2, \tag{1.10}$$

and then calculated, knowing the initial concentration of A (A_0) and its concentration change A_t over time:

$$-\int_{[A]_0}^{[A]_t} \frac{d[A]}{[A]^2} = k_+ \int_0^t dt. \tag{1.11}$$

As a result, we obtain:

$$\frac{1}{[A]_t} = k_+ t + \frac{1}{[A]_0}. \tag{1.12}$$

This equation can be visualized as a linear function (Figure 1.8), where the slope corresponds to the rate constant k_+, and the intercept with the y-axis is $1/[A_0]$. The characteristic timescale of this reaction can be described by the half-time ($t_{1/2}$), defined as the time required for the reactant concentration to decrease to half of its initial value. For a second-order reaction, the half-time is given by:

$$t_{1/2} = \frac{1}{k_+[A]_0}, \tag{1.13}$$

indicating an inverse relationship with the initial concentration, such that higher initial reactant concentrations lead to shorter half-times.

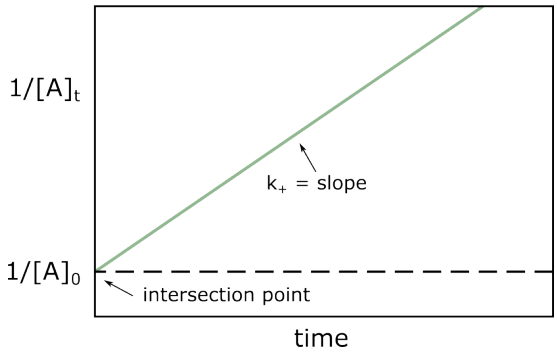

FIGURE 1.8: Visualization of Equation 1.12, where k_+ represents the slope of the line, and $1/[A_0]$ is the y-intercept.

1.4 Fluorescence Mechanisms and Spectra

Luminescence refers to the spontaneous emission of photons from electronically excited states, not driven by thermal energy. This phenomenon can result from chemical reactions, electromagnetic excitation, mechanical stress, or structural changes in crystalline materials. Luminescence is further classified into fluorescence and phosphorescence, based on the nature of the electronic transitions and the spin states involved.

The electron transitions and energy dissipation pathways in fluorescence and phosphorescence can be illustrated using the Jablonski diagram (Figure 1.9).[64] Upon absorption of a photon, an electron transitions from the ground state S_0 to an excited singlet state S_1 or S_2. This absorption process occurs on the femtosecond scale (10^{-15} seconds).[65] Depending on the energy absorbed, the electron may populate higher vibrational levels of S_1 or S_2, followed by non-radiative relaxation processes such as internal conversion and vibrational relaxation. These processes reduce the energy of the system, bringing the electron to the lowest vibrational level of S_1.

Fluorescence emission occurs when the electron returns from S_1 to S_0, releasing energy in the form of a photon. This radiative process is rapid, with fluorescence lifetimes typically in the range of 10^{-8} to 10^{-9} seconds.[60] The emitted photons are of lower energy (longer wavelength) than the absorbed photons due to energy loss during non-radiative relaxation, a phenomenon

known as the Stokes shift.[66] The resulting emission spectrum is broad, reflecting the thermal motion and vibrational coupling of the fluorophore.

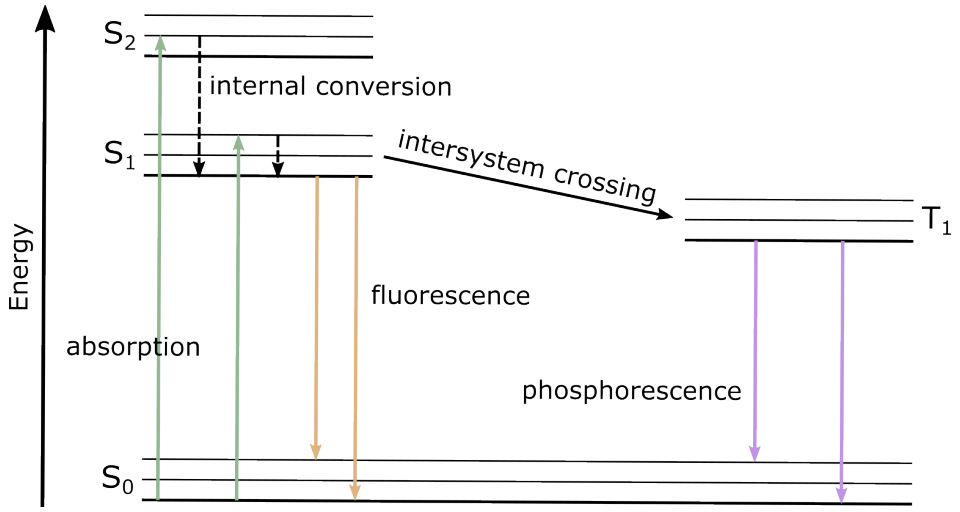

FIGURE 1.9: The Jablonski diagram illustrating the electronic processes occurring in a molecule with fluorescent properties. S_0 represents the ground state, S_1 and S_2 are excited singlet states, and T_1 is the excited triplet state. Photon absorption is marked with a green line, fluorescence with a yellow line, and phosphorescence with a purple line.

Phosphorescence involves a more complex sequence of transitions. Following intersystem crossing, an electron in the S_1 state transitions to the triplet state T_1, where the spin orientation changes. Due to the "forbidden" nature of the spin transition, the lifetime of the triplet state is significantly longer, ranging from milliseconds to seconds or even longer. Phosphorescence emission, therefore, occurs on a much slower timescale than fluorescence and is often observable in the absence of external excitation.

The spectral properties of fluorescence and phosphorescence are influenced by the chemical structure of the emitting molecule (fluorophore) and its surrounding environment. Vibrational relaxation and thermal motion result in a broadening of the emission spectrum, with the Stokes shift determining the energy difference between absorption and emission peaks (Figure 1.10). The proximity of vibrational levels within the ground state also contributes to the spectral characteristics, influencing the efficiency and wavelength of emitted photons.[67]

Fluorescence spectra are further affected by the solvent environment, as interactions between the fluorophore and solvent molecules can shift the energy levels of the excited states. For example, the absorption and emission peaks may shift depending on the polarity or viscosity of the solvent, altering the spectral properties of the fluorophore.[68] These factors are critical for optimizing fluorescence-based techniques in experimental settings.

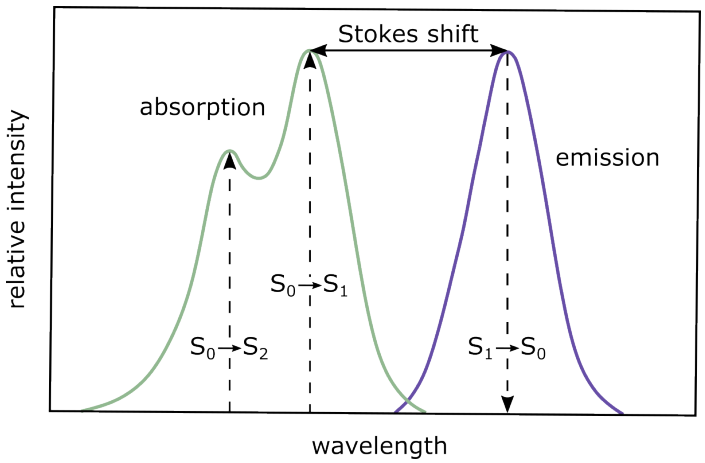

FIGURE 1.10: The diagram of photon absorption spectra to singlet states S_1 and S_2 (green line) and photon emission from the singlet state S_1 (purple line) with the Stokes shift.

Fluorescence is a ubiquitous phenomenon, observed in both natural and synthetic systems. In biological systems, it plays a vital role in the study of cellular and molecular processes. Fluorescence spectroscopy and microscopy have become indispensable tools in modern research, enabling the visualization of intracellular structures, molecular interactions, and dynamic processes in real time.[69] These techniques are particularly valuable for tracking the movement of biomolecules, analyzing metabolic pathways, and investigating structural changes in cells and tissues.[70, 71]

1.5 Experimental Techniques

1.5.1 Confocal and Fluorescence Microscopies

Optical microscopes were the first instruments developed to magnify and visualize biological samples using light transmitted through an optical system. These devices enable the observation of most plant, animal, and bacterial cells, making them fundamental tools in biological research. They are widely employed for monitoring cellular processes, such as movement and physiological changes, in living samples. The advantages of optical microscopes include low cost, ease of use, and the ability to examine live specimens without extensive preparation. However, their utility is limited by the requirement for thin samples to ensure light penetration and, in some cases, the need for chemical fixation techniques that may alter the native properties of the sample.

One of the most significant advancements in optical microscopy is fluorescence microscopy, which utilizes filters to selectively capture emitted and excited light from fluorescently labeled molecules. This technique has enhanced the ability to study specific molecular components in biological systems. Recent developments have focused on improving the standardization and reproducibility of fluorescence microscopy, ensuring consistent and reliable results across different laboratories.[72]

Building on this foundation, confocal microscopy provides further refinement by enabling the acquisition of high-resolution images from specific optical planes within a three-dimensional sample. Unlike traditional microscopes, which integrate signals from all focal planes, confocal microscopes selectively focus on a single plane, thereby eliminating out-of-focus light and enhancing image contrast and resolution. The core innovation of confocal microscopy lies in using a pinhole aperture positioned in front of the detector. This aperture blocks light from regions outside the focal plane, ensuring that only in-focus light contributes to the final image. This design enables point-by-point scanning of the sample, which is typically illuminated by a laser. The resulting data can be used to reconstruct high-resolution two-dimensional images or three-dimensional representations of the sample.[73]

Confocal microscopy is particularly valuable in fields such as cell biology, neuroscience, and biophysics, where precise spatial and temporal resolution is required. It is commonly employed to study the localization of specific proteins, interactions between molecules, and structural dynamics in live cells. Furthermore, the ability to acquire optical sections in the z-axis allows for the construction of detailed three-dimensional models of tissues or organelles, providing insights that are not achievable with traditional optical microscopes.

A confocal microscope operates by directing a laser beam of a specific wavelength through an optical system, including a pinhole aperture. The laser light is reflected by a dichroic mirror, which selectively transmits and reflects light based on its wavelength. This beam is then focused onto the sample, where it excites fluorophores, causing them to emit light at a longer wavelength. The emitted light travels back through the optical system and is refocused by lenses onto the optical axis. The pinhole aperture ensures that only light from the focal plane reaches the detector, while out-of-focus light is blocked. The fluorescent signal is then passed through emission filters to isolate the desired wavelength before reaching the detector, typically a photomultiplier tube or a charge-coupled device (CCD). The detected signal is digitized and processed to generate a final image, which is displayed on a monitor. The construction diagram of the confocal microscope is shown in Figure 1.11.

Despite its many advantages, confocal microscopy has several limitations. The equipment is costly and requires specialized training for operation and maintenance. Imaging times are longer compared to traditional optical microscopy due to the point-by-point scanning process. Additionally, while confocal microscopes provide higher resolution than standard optical microscopes, their resolution remains lower than that of electron microscopy. However, confocal microscopy compensates for this limitation by enabling the observation of live samples and real-time processes, which are not feasible with electron microscopy.

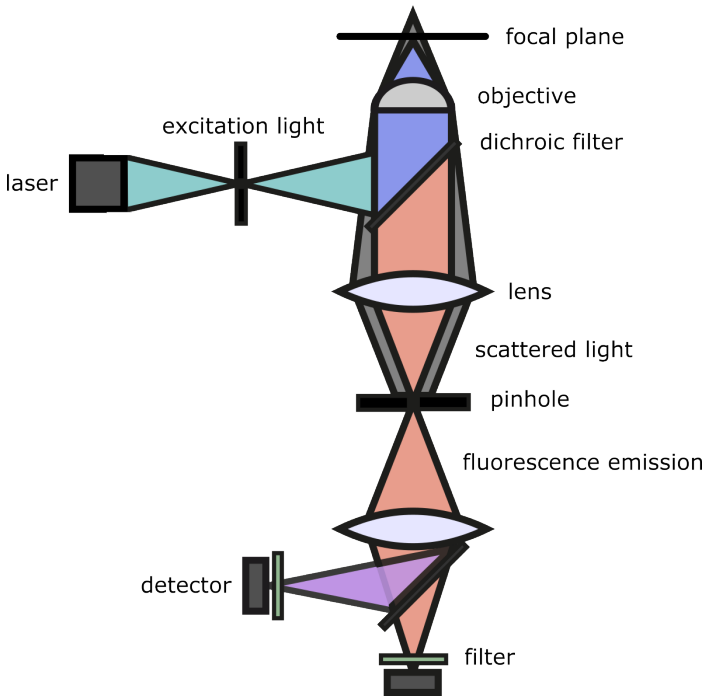

FIGURE 1.11: Construction diagram of a confocal microscope.

1.5.2 Fluorescence Correlation Spectroscopy

Fluorescence correlation spectroscopy (FCS) is a quantitative technique used to study the dynamics and interactions of biomolecules, including DNA, RNA, and proteins. It enables the analysis of molecular diffusion, binding, and conformational changes in solution at nanomolar concentrations and with single-molecule sensitivity. A key advantage of FCS is that it does not require molecular immobilization, which is often necessary in other fluorescence-based techniques and can alter biomolecular behavior. Immobilization, while preventing diffusion, often leads to photobleaching due to prolonged exposure to high-intensity illumination, thereby limiting observation times [74, 75]. FCS overcomes this limitation by combining confocal microscopy with temporal correlation analysis of fluorescence intensity fluctuations. These fluctuations arise as fluorescent molecules stochastically diffuse in and out of a small, optically defined observation volume.

The detection volume in FCS is formed by the focused laser excitation and the confocal pinhole, and is typically on the order of femtoliters (10^{-15} L). It is three-dimensional and approximately ellipsoidal in shape, characterized by a Gaussian intensity profile. The dimensions of this confocal volume are described by the lateral radius ω_1 (equal in the x- and y-directions) and the axial radius ω_2 along the z-axis (Figure 1.12). The anisotropy of the confocal geometry is expressed by the structural parameter κ:

$$\kappa = \frac{\omega_2}{\omega_1}. \tag{1.14}$$

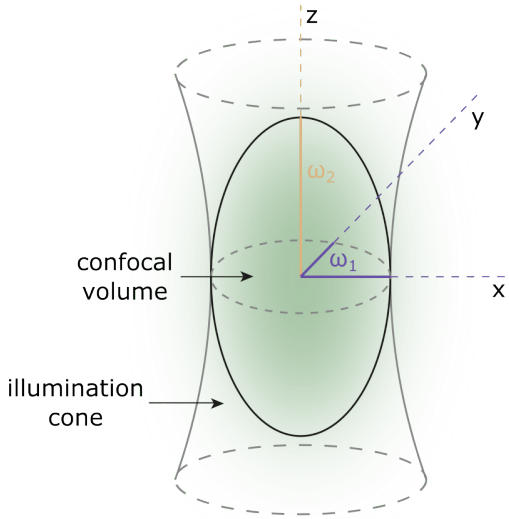

FIGURE 1.12: Confocal volume and illumination cone with radii descriptions.

Because fluorescence intensity gradually decreases toward the edges of the detection volume, an effective volume V_{eff} is defined to represent the region from which most of the fluorescence signal originates:

$$V_{\text{eff}} = \pi^{3/2}\omega_1^2\omega_2. \tag{1.15}$$

This effective volume depends on the optical setup, including the numerical aperture of the objective, laser wavelength, and alignment of the excitation and detection paths. Accurate knowledge of V_{eff} is essential for quantitative

interpretation of FCS data, particularly for calculating molecular concentrations.

To determine V_{eff} experimentally, FCS measurements are first performed on a fluorescent reference dye with a well-characterized diffusion coefficient in aqueous solution, such as Rhodamine B or Alexa Fluor 488. Fitting the measured autocorrelation function to a standard diffusion model yields the characteristic diffusion time τ_D. The lateral radius ω_1 is then calculated from the known diffusion coefficient D_{ref}:

$$\omega_1 = \sqrt{4D_{\text{ref}}\tau_D}. \tag{1.16}$$

The axial radius ω_2 is subsequently obtained from the structural parameter κ, and the effective volume is recalculated as:

$$V_{\text{eff}} = \pi^{3/2}\omega_1^3\kappa. \tag{1.17}$$

Once calibrated, the FCS setup can be used to analyze unknown samples. Fluorescent molecules diffusing in and out of the confocal volume generate temporal fluctuations in fluorescence intensity. These fluctuations occur because the number of molecules in the detection volume is small – typically between 1 and 10. Molecules with different diffusion coefficients exhibit distinct fluctuation patterns: faster molecules (D_1) cause rapid, short-lived fluctuations, while slower ones (D_2) lead to longer-lasting intensity changes (Figure 1.13).

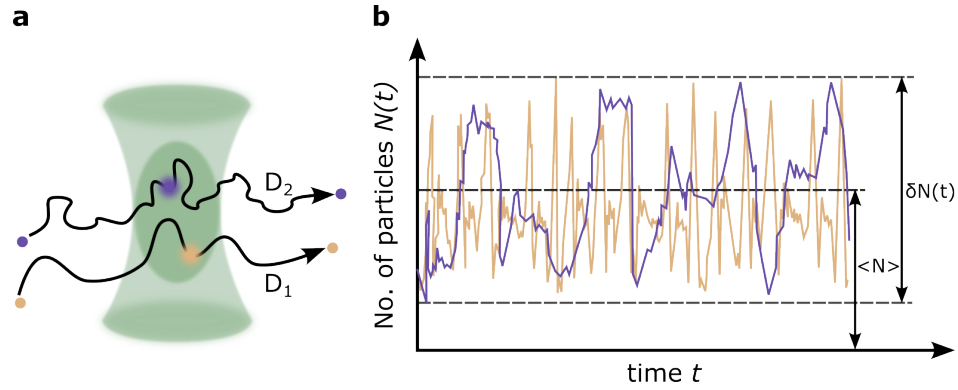

FIGURE 1.13: **(a)** Confocal volume with two types of molecules passing through it, each having different diffusion coefficients. **(b)** Time trace showing changes in the number of molecules detected within the focal volume over time. The yellow signal corresponds to the faster molecule with a diffusion coefficient D_1, while the purple signal represents the slower molecule with a diffusion coefficient D_2.

The fluorescence intensity $I(t)$ is proportional to the number of molecules $n(t)$ in the observation volume:

$$n(t) = \langle n \rangle + \Delta n(t), \qquad I(t) = \langle I \rangle + \delta I(t), \tag{1.18}$$

where $\langle n \rangle$ and $\langle I \rangle$ denote the average particle number and intensity, and $\Delta n(t)$ and $\delta I(t)$ are fluctuations around these averages.

To extract quantitative information, these fluctuations are analyzed using the autocorrelation function:

$$G(\tau) = \frac{\langle I(t) I(t+\tau) \rangle}{\langle I(t) \rangle^2}, \tag{1.19}$$

which describes the time-dependent correlation of intensity fluctuations at delay time τ. For a single species undergoing free 3D diffusion, such as single-stranded DNA, the autocorrelation function follows:

$$G(\tau) = \frac{1}{N} \cdot \left(1 + \frac{\tau}{\tau_D}\right)^{-1} \cdot \left(1 + \frac{\tau}{\kappa^2 \tau_D}\right)^{-1/2}, \tag{1.20}$$

where N is the average number of molecules in the confocal volume and τ_D is the characteristic diffusion time. The diffusion coefficient D is then calculated

as:

$$D = \frac{\omega_1^2}{4\tau_D}. \tag{1.21}$$

In addition to diffusion, the initial amplitude of the autocorrelation function provides access to (i) molecular concentration:

$$C = \frac{N}{N_A V_{\text{eff}}}, \tag{1.22}$$

where N_A is Avogadro's number, and (ii) molecular brightness.

1.5.3 Molecular Brightness Analysis

Molecular brightness is a key parameter for quantifying the luminescent behavior of individual molecules in fluorescence-based techniques. In photophysics, the intrinsic brightness B of a fluorophore is defined as the product of its molar absorption coefficient $\varepsilon(\lambda)$ and quantum yield $\phi(\lambda)$:

$$B = \varepsilon(\lambda) \cdot \phi(\lambda). \tag{1.23}$$

This value characterizes how efficiently a molecule converts absorbed photons into emitted fluorescence but does not account for experimental variables such as molecular concentration or detection volume.

In the context of fluorescence correlation spectroscopy (FCS) and related techniques, the more practical quantity is the *molecular brightness* χ, which is defined as the average photon count rate per molecule:

$$\chi = \frac{\langle I \rangle}{N}, \tag{1.24}$$

where $\langle I \rangle$ is the average fluorescence intensity (in photons per second), and N is the average number of fluorescent molecules in the confocal volume. Molecular brightness reflects not only the intrinsic properties of the fluorophore, but also the local environment, including quenching, complexation, or changes in conformation.

Changes in molecular brightness can be used to study biomolecular interactions, such as the formation of complexes. Consider the reversible binding

reaction:

$$A + B \leftrightharpoons AB,$$

where A is a fluorescent molecule and B is a non-fluorescent binding partner. The molecular brightness of free A is denoted α, while the brightness of the AB complex is γ. If the fluorescence of A is altered upon binding (due to changes in quenching or quantum yield), the total fluorescence intensity reflects the population-weighted contribution from both species.

The Hołyst group has developed a method known as Molecular Brightness Analysis (MBA) that uses this principle to extract equilibrium binding constants from brightness changes measured across a concentration series [21].

Initially, the fluorescence count rate χ is measured in a solution containing only A, and can be written as:

$$\chi = V_0 \cdot \alpha \cdot C_A, \tag{1.25}$$

where V_0 is the calibrated confocal volume, α is the molecular brightness of free A, and C_A is its concentration.

Upon titration with increasing concentrations of B, the complex AB forms, altering the observed count rate. At equilibrium, the fluorescence signal includes contributions from both A and AB:

$$\chi = V_0 \cdot (\alpha \cdot C_A^{\text{eq}} + \gamma \cdot C_{AB}^{\text{eq}}), \tag{1.26}$$

where C_A^{eq} and C_{AB}^{eq} are the equilibrium concentrations of the free and complexed fluorophore, respectively.

The molecular brightness values α and γ correspond to the free and bound states of A, respectively. These values are obtained from FCS measurements by analyzing fluorescence intensity fluctuations and the average number of fluorescent molecules, using the relation $\chi = \langle I \rangle / N$. This approach ensures that observed changes in count rate reflect genuine photophysical or structural changes upon binding, rather than differences in concentration. In practice, the value of γ can also be determined independently by measuring the fluorescence signal in the presence of a large excess of B (typically 10–50-fold

higher than A), where nearly all fluorophores are expected to be in the complexed form.

The equilibrium constant for the 1:1 binding reaction is defined as:

$$K = \frac{C_{AB}^{\mathrm{eq}}}{C_A^{\mathrm{eq}} \cdot C_B^{\mathrm{eq}}} = \frac{C_{AB}^{\mathrm{eq}}}{(C_A^0 - C_{AB}^{\mathrm{eq}})(C_B^0 - C_{AB}^{\mathrm{eq}})}, \tag{1.27}$$

where C_A^0 and C_B^0 are the total initial concentrations of A and B, respectively.

Substituting this relationship into Equation 1.26 yields the final expression used in MBA:

$$\chi = V_0 \cdot \alpha \cdot (C_A^0 - C_{AB}^{\mathrm{eq}}) \cdot \left[1 + \frac{\gamma}{\alpha} \cdot K \cdot (C_B^0 - C_{AB}^{\mathrm{eq}})\right]. \tag{1.28}$$

To experimentally determine K, a series of measurements are conducted at varying C_B^0/C_A^0 ratios. For each point, the total count rate χ is measured and the data are fit using Equation 1.28. This allows the extraction of both K and the molecular brightness values α and γ when necessary. The method is highly sensitive, enabling quantification of binding equilibria at nanomolar or even picomolar concentrations.

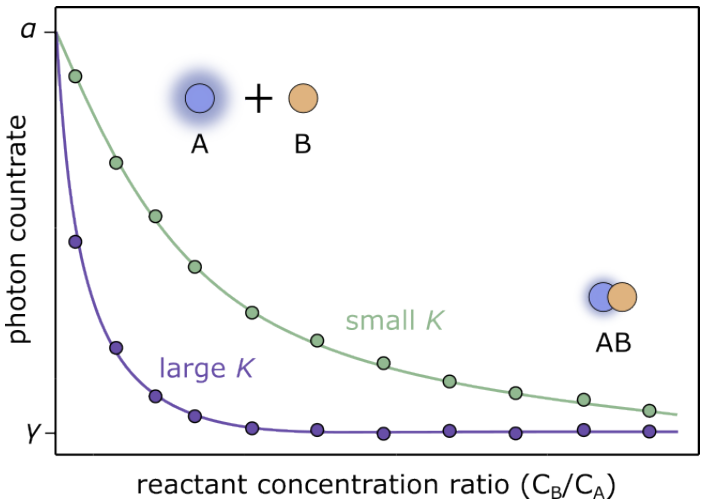

FIGURE 1.14: Example plot showing the measured count rate during AB complex formation, fitted using Equation 1.28 for the case where $\alpha > \gamma$. As the complex forms, the count rate decreases. A greater decrease in count rate for a given C_B/C_A ratio indicates a stronger binding affinity (higher equilibrium constant K).

1.5.4 Förster Resonance Energy Transfer

While MBA allows the determination of equilibrium constants K with only one fluorescently labeled reactant, additional insight can be gained by labeling the second reactant at a defined site with a spectrally compatible dye. This enables the use of Förster Resonance Energy Transfer (FRET), a powerful technique for probing molecular proximity at the nanometer scale.

FRET is based on a non-radiative energy transfer mechanism between two fluorophores: a donor, which absorbs excitation light and transfers energy via dipole-dipole interactions, and an acceptor, which receives this energy and may re-emit it as fluorescence. The efficiency of energy transfer (E) depends strongly on the distance r between the donor and acceptor, following the characteristic relation:

$$E = \frac{1}{1 + \left(\frac{r}{R_0}\right)^6}, \tag{1.29}$$

where R_0 is the Förster distance – the separation at which $E = 50\%$.

In addition to distance, FRET efficiency is influenced by the relative orientation of the donor and acceptor dipole moments, the local dielectric environment, and particularly by the degree of spectral overlap between the donor's emission and the acceptor's absorption spectra. This overlap is quantified by the spectral overlap integral J, defined as:

$$J = \int_0^\infty F_D(\lambda) \cdot \varepsilon_A(\lambda) \cdot \lambda^4 \, d\lambda, \tag{1.30}$$

where $F_D(\lambda)$ is the normalized donor emission spectrum, $\varepsilon_A(\lambda)$ is the molar extinction coefficient of the acceptor, and λ is the wavelength. A larger J value indicates a higher probability of energy transfer, making fluorophore pair selection a critical consideration in FRET experimental design.

Due to its steep distance dependence ($E \propto r^{-6}$), FRET functions as a highly sensitive molecular ruler capable of detecting changes in donor–acceptor separation over the 1–10 nm range. It is widely applied in studies of protein-protein interactions, nucleic acid hybridization, and conformational changes in biomolecular complexes. However, a key limitation is the requirement for dual fluorophore labeling, which demands careful design to ensure that both

dyes remain within the Förster radius after binding.[76]

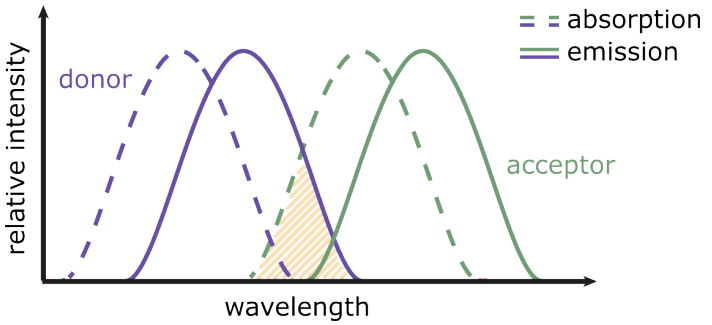

FIGURE 1.15: Example absorption (dashed) and emission (solid) spectra for a donor (purple) and acceptor (green) fluorophore. The yellow region indicates the spectral overlap between the donor emission and acceptor absorption, which is essential for efficient FRET.

1.6 Microfluidics

1.6.1 Introduction to Microfluidics

Microfluidics is a technology that enables the precise control and manipulation of fluids within microscale channels, typically measuring tens to hundreds of micrometers in width. At these length scales, fluid behavior is governed by laminar flow, surface tension, and capillary forces, enabling predictable transport, low reagent consumption, and integration of multiple analytical steps onto a single device [77, 78]. These characteristics have led to the development of so-called lab-on-a-chip systems, which consolidate sample preparation, reaction, and detection processes into compact platforms [79].

In the context of biomolecular analysis, microfluidic systems offer unique advantages, including reduced sample volumes, increased throughput, and enhanced compatibility with optical detection methods such as FCS and MBA[80, 81]. Their ability to create stable, reproducible droplet-based environments further enables reaction compartmentalization and real-time monitoring under well-defined conditions.

In this thesis, microfluidic technology was leveraged to address critical limitations in the manual determination of DNA hybridization equilibria –

specifically, the time-intensive sample preparation, low throughput, and high reagent consumption of standard FCS and MBA protocols.

1.6.2 Fundamental Principles of Microfluidics

At the microscale, fluid dynamics deviate significantly from macroscopic behavior. Due to the low Reynolds numbers ($Re < 1$), flows are typically laminar and highly predictable, with viscous forces dominating over inertial effects [77]. In such regimes, mixing between fluid streams is governed predominantly by molecular diffusion, prompting the development of strategies to enhance mixing, such as the use of serpentine geometries, chaotic advection, or external fields (e.g., magnetic or acoustic) [82].

The high surface-area-to-volume ratio characteristic of microfluidic channels leads to a dominant role of interfacial forces. Surface tension, capillary action, and wetting behavior govern droplet formation and fluid motion, and can even drive passive flow in pump-free systems – a property particularly relevant for portable and resource-efficient designs [78].

Microfluidic transport processes include the transfer of mass, momentum, and heat. The small characteristic lengths of microchannels reduce diffusion distances and thermal equilibration times, enhancing the control of reaction kinetics [83]. Additionally, electrokinetic phenomena such as electroosmosis and electrophoresis enable precise manipulation of ionic species and biomolecules using electric fields, and are widely used in microchip-based separations and bioanalytical assays [80].

The fabrication of microfluidic devices typically involves either subtractive methods, such as photolithography and etching on silicon or glass, or soft lithography using elastomers like polydimethylsiloxane (PDMS), which offers excellent optical transparency and biocompatibility. More recently, additive manufacturing techniques (e.g., 3D printing) have enabled rapid prototyping of complex channel geometries and integration of multifunctional components [84, 85]. The choice of fabrication method depends on the desired resolution, material compatibility, and application-specific requirements.

1.6.3 Applications of Microfluidics

Microfluidic technologies have been applied extensively across the physical, chemical, and life sciences. In biomedical diagnostics, they enable the detection of disease biomarkers with high sensitivity and minimal sample volume, supporting point-of-care applications in both clinical and resource-limited settings [86]. For example, paper-based microfluidic platforms using colorimetric assays can be interpreted by smartphones for the rapid identification of bacterial pathogens such as *E. coli*.

In molecular biology and biotechnology, microfluidics facilitates high-throughput screening and single-cell analysis. Droplet-based platforms allow the compartmentalization of individual cells or molecules for transcriptomic profiling, revealing cellular heterogeneity in complex systems [87]. Organ-on-a-chip systems that mimic the architecture and function of human tissues are increasingly used in drug screening, offering more physiologically relevant alternatives to traditional 2D cell culture [88, 89].

Microfluidic integration of nucleic acid amplification techniques – such as polymerase chain reaction (PCR) and digital PCR – has significantly improved the speed, efficiency, and quantitative resolution of genomic assays [81]. Additionally, microfluidic reactors support continuous-flow synthesis under well-controlled conditions, facilitating the generation of monodisperse nanoparticles and enabling novel reaction schemes [79].

Despite these advances, key challenges remain in scaling up device fabrication, achieving reproducible performance, and integrating fluidic, optical, and electronic components into fully autonomous systems. Future developments are expected to leverage hybrid manufacturing strategies, new biocompatible materials, and nanofluidic innovations to expand the functionality of microfluidic platforms [90]. In this thesis, microfluidics is not treated as an end in itself but as a means of enabling the semi-automated, high-throughput quantification of biomolecular interactions.

Chapter 2

Materials & Methods

This section describes the compounds, liquids, and other materials used, as well as the methods and configurations of setups.

2.1 Materials

2.1.1 Oligonucleotides

Measurements were conducted on 13- (5′ ATC GTG TAG GCA T 3′, 5′ ATG CCT ACA CGA T 3′ – Systems 1 and 3) and 20-base-pair-long (5′ ATC GTT GGA GCT TGA GGC AT 3′, 5′ ATG CCT CAA GCT CCA ACG AT 3′ – Systems 2 and 4) DNA strands (IBA GmbH, Germany), and used without further purification (Figure 2.1). The hybridization was investigated using FRET and MBA. Accordingly, distinct pairs of reactants were prepared. For the FRET measurements, oligonucleotides were labeled with two fluorescent dyes, Atto488 and Atto647, each conjugated to a different strand and positioned at the same terminus upon hybridization. For the MBA experiments, one reactant was labeled with Atto488, while the complementary strand remained nonfluorescent. The designed sequences prevent the formation of secondary structures and are shown in Figure 2.1. Aliquots were stored at a stock concentration of 100 µM in standard Tris-EDTA buffer at -20 °C. Before measurements, aliquots were diluted in various aqueous solutions at pH 7.4, containing 0.002% Tween 20, and stored at 4 °C for 48 hours to allow the reactants to reach equilibrium. The surfactant was added to maintain oligonucleotides in the solution and prevent their accumulation at the

water–glass or water-air interfaces.[91] All measurements were conducted at 25 °C.

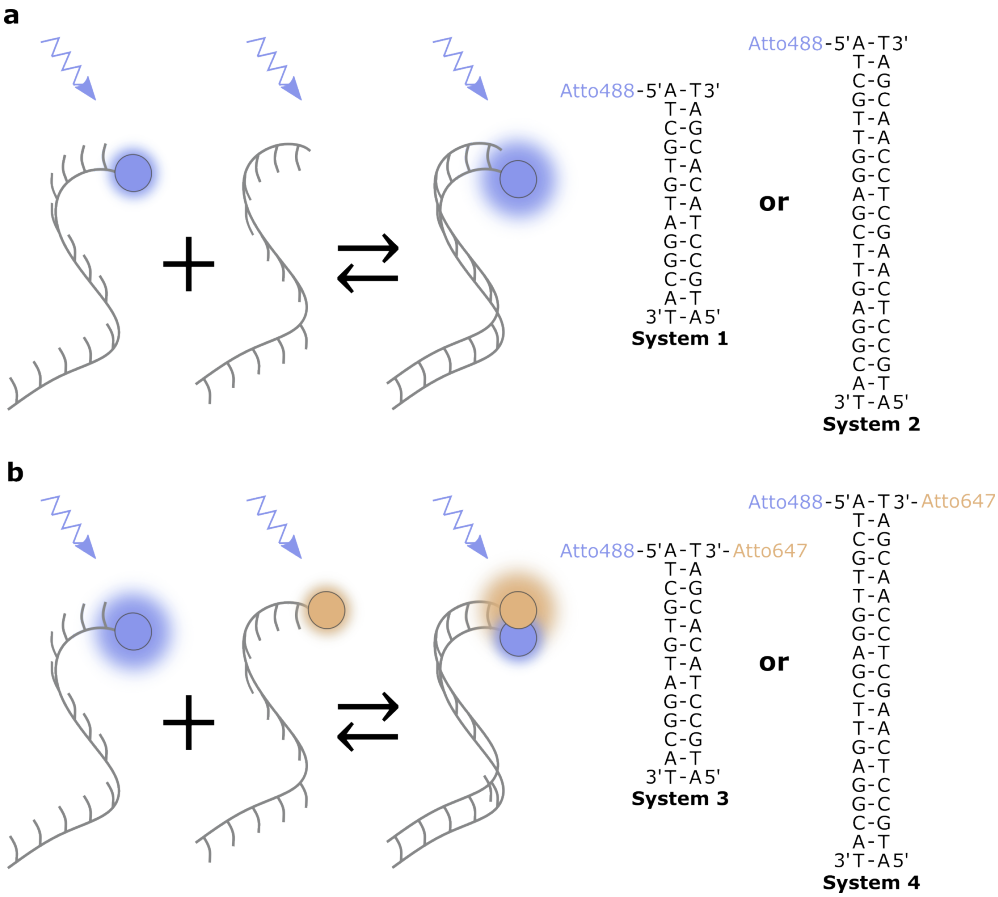

FIGURE 2.1: Oligonucleotide sequences of 13 and 20 base pairs in length were studied in this work. **(a)** Reactant system designed for MBA measurements, in which fluorescence intensity increased upon hybridization (Systems 1 and 2). **(b)** Reactant system designed for FRET measurements, where hybridization was followed in energy transfer from the donor to the acceptor fluorophore (Systems 3 and 4). Consequently, the fluorescence intensity of the Atto488-labeled DNA strand decreased, while the intensity of the Atto647-labeled strand increased. Arrows indicate the excitation of the samples using a 485 nm laser.

2.1.2 Catalysts

The association rate of oligonucleotides was investigated in relation to the charge type and distribution over co-solubilized molecules. The positively

charged compounds included arginine with nine monomers - arginine-9 (Arg-9, Anaspec, Belgium), cetrimonium chloride (CTAC, TCI, Belgium), cetylpyridinium chloride (CPC, Sigma-Aldrich, USA), and benzethonium chloride (BTC, Sigma-Aldrich, USA). Sodium dodecyl sulfate (SDS, GmbH, Germany) was used as a negatively charged catalyst, while Brij L23 (Sigma-Aldrich, USA) served as a neutral one. The chemical structures of these molecules are presented in Figure 2.2. All compounds were dissolved in aqueous solution. The surfactants were stored at 5 °C, whereas arginine-9 was maintained at -20 °C and thawed before use.

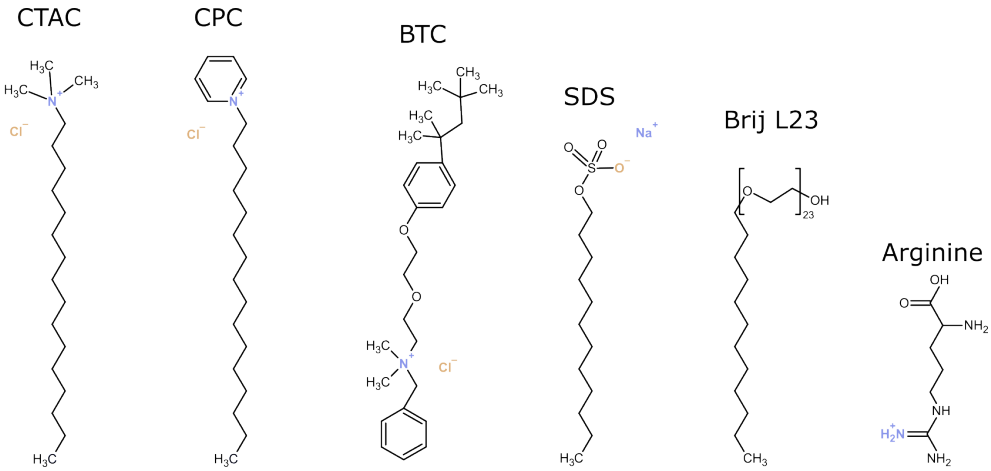

FIGURE 2.2: The chemical structures of the catalyst molecules. The positive charge is highlighted in blue, while the negative charge is indicated in orange.

2.1.3 Crowders

To mimic the cellular environment, the oligonucleotide hybridization was studied in the presence of crowders such as ethylene glycol (EG) and polyethylene glycols (PEGs) of varying molar masses, including PEG 200, PEG 400, PEG 600, PEG 1000, PEG 1500, PEG 3000, PEG 6000, PEG 12000, PEG 20000, and PEG 35000. All the chemicals were purchased from Sigma-Aldrich, USA, and stored at room temperature.

2.1.4 Solutions

To maintain pH stability or modify the ionic strength of aqueous systems, the following solutions were used: phosphate-buffered saline (PBS), sodium phosphate buffer (PB-Na), and potassium phosphate buffer (PB-K). A 0.5 M PB-Na stock solution was prepared by dissolving 0.573 g of NaH_2PO_4 and 7.2415 g of $Na_2HPO_4{\cdot}12H_2O$ in Mili-Q water to a final volume of 50 mL, followed by pH adjustment to 7.4. Similarly, a 1 M PB-K stock solution was prepared by mixing 32.08 mL of 1 M KH_2PO_4 with 7.92 mL of 1 M K_2HPO_4, after which the pH was measured and adjusted to 7.4.

To validate the microfluidic setup, aqueous droplets were infused with food dyes, including Allura Red AC (E129), Brilliant Blue FCF (E133), and Quinoline Yellow WS (E104). For droplet formation, Novec 7500 (3M, USA) containing 2% fluorosurfactant (RAN Biotechnologies, USA) was used as the oil phase. The surfactant was added to stabilize aqueous droplets and prevent them from adhering to the channel walls.

2.2 Methods

2.2.1 Confocal Microscope Setup

Reactant properties and interactions were assessed using a Nikon C1 inverted confocal microscope equipped with a PicoQuant LSM module, integrated with the PicoHarp 300 Time-Correlated Single-Photon Counting (TCSPC) system. Measurements were performed in glass-bottom plates (ibidi GmbH, Germany) or directly in droplets trapped within the core of the detection unit. The detection unit or plate was positioned above the objective, and the focal volume parameters were defined using a Nikon PlanApo 60× water immersion lens (NA = 1.2). The focal volume was set at a depth of 10 µm from the glass bottom and remained fixed during measurements.

The focal volume size was estimated by system calibration using Rhodamine 110 (Sigma-Aldrich, USA) and fluorescence correlation spectroscopy (FCS) measurements. Sample excitation was achieved using a pulsed diode laser (PicoQuant GmbH, Germany) operating at two wavelengths (485 nm and 636 nm) with a pulse interval excitation scheme. The laser operated at a

pulse frequency of 40 MHz, with an optimized power of 40 µW, measured at the entry point of the objective using a power meter (PM 100, Thorlabs).

For the double-labeled system, fluorescence intensity fluctuations were recorded in two detection channels using a dichroic mirror (T635). In the first channel (CH1), the signal acquisition was synchronized with the 485 nm laser pulse, while in the second channel (CH2), detection followed excitation by the 636 nm laser. A climate-controlled chamber (temperature and humidity, OkoLab, Italy) enclosed the setup to minimize background noise and maintain a constant temperature of 25 $\pm$ 0.5 °C. The emitted fluorescence was detected by a single-photon avalanche photodiode (PerkinElmer Optoelectronics, Canada), with signal transmission through a 645 nm long-pass filter for CH2 and a 525/50 nm bandpass filter for CH1. For single-labeled systems, photon detection was restricted to a single channel using the 485 nm laser, a 488 nm long-pass filter or 525/50 nm bandpass filter, and the same laser power and pulse frequency settings. Data acquisition and analysis were performed using a custom Python script. The microscope system was controlled via the PicoQuant Sepia II laser controller and SymphoTime 64 software.

2.2.2 Microfluidic Setup

The fluid motion was controlled using low-pressure Nemesys 290 N syringe pumps (Cetoni GmbH, Germany), which were integrated with an HSZ-645TR stereoscope (Huvitz, South Korea) and a UI-3274LE-C-HQ CCD camera (IDS, Germany). The oil phase (OP) and aqueous phases (APs) were introduced into 1 mL glass syringes (Hamilton, USA) and connected to the droplet-on-demand unit (DODU) via polytetrafluoroethylene (PTFE) tubing (Bola GmbH, Germany) with an inner diameter of 0.8 mm and an outer diameter of 1.6 mm. Droplet formation was regulated by a custom-written Python script, which processed real-time image feedback from a camera to control four pumps – three for distinct APs and one for the OP. This automated procedure minimized the unintended mixing of APs due to potential liquid leakage at interconnections and ensured consistent spacing between consecutive droplets.

Droplet On-Demand Unit (DODU). The system was fabricated using a CNC milling machine (Ergwind, Poland) equipped with a 0.4 mm end mill (FR208, inGraph, Poland), and the geometries were engraved into a single 4 mm polycarbonate (PC) plate (Makrolon, Bayer AG, Germany). A second 4 mm PC plate, containing inlet and outlet holes, was bonded to seal the channels. To ensure proper alignment, steel pins with a diameter of 0.8 mm were inserted into auxiliary holes, and the plates were fused using a hot press at 135 °C and 2 bars for 15 minutes. Subsequently, the channels were surface-modified by introducing Novec 1720 (3M, USA) under a vacuum of 15 millibars for 2 minutes, followed by thermal treatment in an oven at 90 °C for 15 minutes. To facilitate controlled droplet coalescence, an electromagnetic field was applied by embedding wire electrodes (UL3239 28AWG with XLPE insulation, rated for 6 kV-DC) into dedicated channels. The APs and the OP were delivered through PTFE tubing (Bola GmbH, Germany), which was flattened at the ends and sealed to the PC plate using 1.2 mm diameter screws with nuts. The outlet Teflon tubing (0.4 mm inner diameter, 0.9 mm outer diameter) was secured in the same manner.

Detection Unit (DU). The system consisted of a polydimethylsiloxane (PDMS) component with pocket channels (P1) bonded to a 0.1 mm microscope cover glass (ESCO, USA) (P2). The detection system was connected to the DODU at the inlet and to the waste at the outlet via PTFE tubing with an inner diameter of 0.4 mm and an outer diameter of 0.9 mm (Bola GmbH, Germany). P1 was fabricated by casting a 10:1 mixture of PDMS base (Sylgard, USA) and curing agent (Sylgard, USA) into a negative mold, followed by curing at 75 °C for 3 hours, similarly to the protocol described by Friend and Yeo.[92] After curing, P1 was removed from the negative mold and exposed to P2 for 1 minute under oxygen plasma treatment in a plasma cleaner (Harrick Plasma, USA) to facilitate bonding. The negative mold was prepared by pouring the same PDMS mixture used for P1 over a polycarbonate mask and curing it under identical conditions. To prevent adhesion, the negative mold was silanized with (3-Aminopropyl)triethoxysilane (Sigma-Aldrich, USA) vapor in a vacuum chamber at 10 millibars for 1 hour before casting P1. The mask itself was fabricated using a CNC milling machine equipped with a 0.4 mm end mill in a 4 mm polycarbonate plate. The geometries of DODU and

DU cores are illustrated in Figure 2.3.

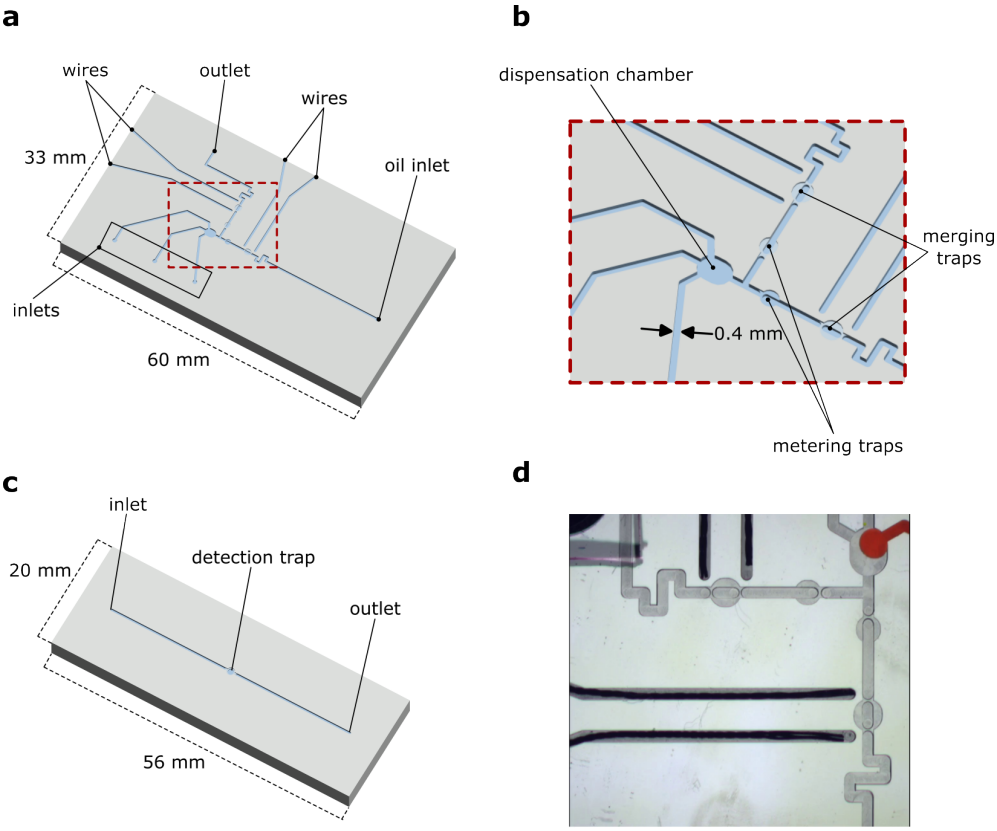

FIGURE 2.3: **(a, b)** Precise geometries of Droplet on Demand Unit (DODU) and **(c)** Detection Unit (DU) cores, and **(d)** image of the fabricated DODU core.

Chapter 3

Results & Discussion

3.1 Association Rate of DNA Oligonucleotides

This section describes the association kinetics of DNA oligonucleotides in aqueous, ionic, and catalyzed environments. A model describing the acceleration of reactions between like-charged DNA strands by oppositely charged molecules in solution is also presented.

3.1.1 Association Rate Constant

The association of complementary DNA strands is described by Equation 1.12. During hybridization, the fluorescent signal of the FRET acceptor increases proportionally to the concentration of the forming duplex. Accordingly, the time-dependent apparent rate constant k_t can be expressed as a function of the fluorescence intensity I_t at time t, and the fluorescence intensity at equilibrium, I_{eq}:

$$\frac{1}{I_{eq} - I_t} = k_t \cdot t + \frac{1}{I_{eq}}. \tag{3.1}$$

To estimate the overall rate constant k, the following rearranged expression was used to determine k_t at each time point:

$$k_t = \frac{I_t}{I_{eq}\left(I_{eq} - I_t\right) t}. \tag{3.2}$$

The overall association rate constant k was then obtained as the weighted mean of k_t values, with the uncertainty determined from the weighted standard error.

3.1.2 Hybridization Rate in Water and Ionic Solution

In pure water, the strong electrostatic repulsion between negatively charged DNA strands prevents hybridization, as each nucleotide carries a single negative charge. To investigate this effect, 13-base-pair oligonucleotides were diluted in pure water containing 0.002% Tween 20 to prevent surface adhesion of oligonucleotides. Both the donor and acceptor fluorophores were prepared at a concentration of 10 nM, and a 4 mm electromagnetic rotor was used to ensure continuous mixing after the acceptor was introduced into the donor solution. The kinetics of DNA duplex formation were monitored using FRET in a double-labeled reactant system in two channels (Section 2.2.1), with fluorescence signals recorded over a 14-day period (Figure 3.1).

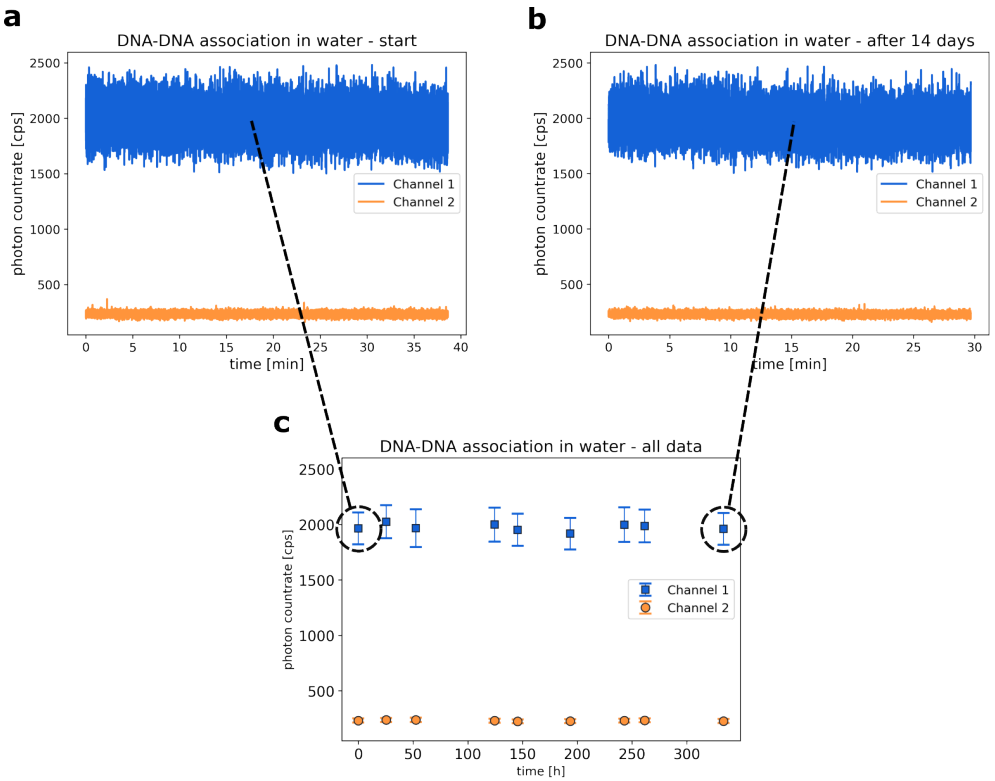

FIGURE 3.1: **(a)** Fluorescence signal of DNAs recorded at the initiation of the measurement and **(b)** after a 14-day incubation period. Channel 1 shows the FRET donor signal, while channel 2 shows the FRET acceptor signal. **(c)** DNA-DNA single-strand hybridization in pure water, presented as an average fluorescence signal. No double-strand formation was observed over a span of 14 days.

No significant changes in fluorescence intensity were observed throughout the experiment, indicating that hybridization did not occur. This lack of reaction progression is attributed to the absence of counterions, which are essential for screening electrostatic repulsion and facilitating strand hybridization. Previous studies have demonstrated that monovalent and divalent cations enable DNA duplex formation by neutralizing the negative charges on the phosphate backbone, effectively reducing electrostatic repulsion between complementary strands.[93] In contrast, in ion-depleted conditions, DNA strands remain strongly repelled, preventing hybridization even over extended timescales.[10] Molecular dynamics simulations have further confirmed that in the absence of sufficient counterions, DNA duplex formation is significantly hindered due to persistent electrostatic interactions.[94] Therefore, in the next step, the association of DNA oligonucleotides in the presence of ions was examined by substituting water with sodium phosphate buffer (PB-Na) and studying reaction speeds at 1 mM and 100 mM concentrations (Figure 3.2).

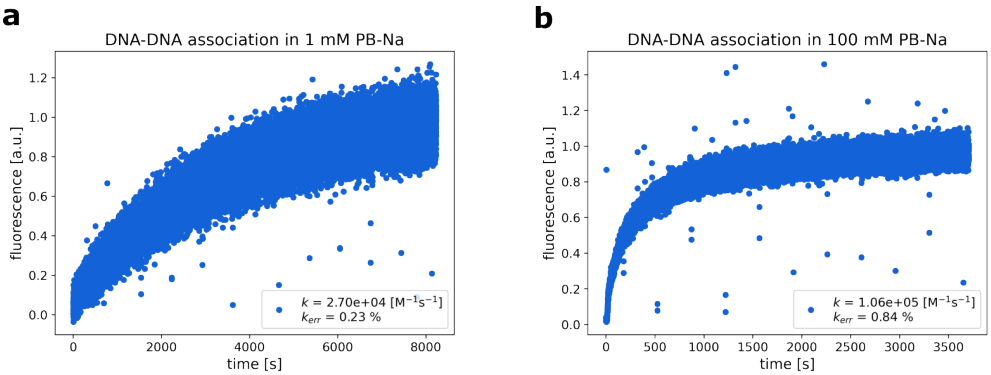

FIGURE 3.2: DNA-DNA double strand formation in **(a)** 1 mM sodium phosphate buffer and **(b)** 100 mM sodium phosphate buffer

The results revealed a significantly higher reaction rate in 100 mM PB-Na ($k = 1.06 \times 10^5$ [$M^{-1}s^{-1}$], Figure 3.2b) compared to 1 mM PB-Na ($k = 2.70 \times 10^4$ [$M^{-1}s^{-1}$], Figure 3.2a). The increased ionic strength in 100 mM PB-Na effectively shields electrostatic repulsion, facilitating hybridization by lowering the energetic barrier for duplex formation. In contrast, 1 mM PB-Na provides less effective charge screening, resulting in slower reaction rates.

These findings confirm the critical role of ionic strength in modulating nucleic acid interactions and suggest that hybridization in ion-free environments is unlikely without additional stabilizing factors.

3.1.3 Enhancing DNA-DNA Association Using Charged Molecules

The DNA-DNA association rate can be enhanced by complex molecules possessing a net charge, such as oligomers, enzymes, and binding sites of proteins.[95, 96] These systems facilitate the formation of transient non-covalent complexes, which partially neutralize the charges of the reactants and bring them into close proximity, thereby increasing the frequency of reactant encounters. Consequently, molecules exhibiting a positive net charge, including nona-arginine (Arg-9), cetyltrimethylammonium chloride (CTAC), benzethonium chloride (BTC), and cetylpyridinium chloride (CPC), were introduced into 1 mM PB-Na buffer with 0.002% Tween. The concentrations of DNA strands were maintained at 10 nM, while the concentrations of catalysts varied.

In the first series of experiments, the DNA-DNA association rate was studied in the presence of Arg-9 at a concentration adjusted to equalize the number of positive charges in solution with the number of negative charges on the reactants. Specifically, arginine was used at 29 nM (26 charges on both DNA strands divided by 9 charges on Arg-9 times 10 nM), followed by 2-, 10-, and 50-fold increments in concentration (58 nM, 0.29 µM, and 1.45 µM).

The presence of Arg-9 significantly enhanced the DNA-DNA association rate compared to phosphate buffer alone, with the k increasing up to approximately 160-fold relative to 1 mM PB and ∼6-fold compared to 100 mM PB (Figure 3.3). Interestingly, the reaction rate remained relatively stable across a wide range of Arg-9 concentrations, with k values varying from 1.65×10^6 to 3.08×10^6 $M^{-1}s^{-1}$, despite a 50-fold difference in concentration. This observation suggests that Arg-9 saturates DNAs at nanomolar levels, where it effectively neutralizes the negative charge of DNA and promotes association. Such behavior aligns with known mechanisms of cationic molecules facilitating nucleic acid interactions, as reported for multivalent cations such as spermidine and poly-L-arginine.[97] These results highlight the remarkable efficiency of

Arg-9 in mediating DNA-DNA interactions, even at minimal concentrations, suggesting its potential as a highly potent DNA-condensing agent.[98]

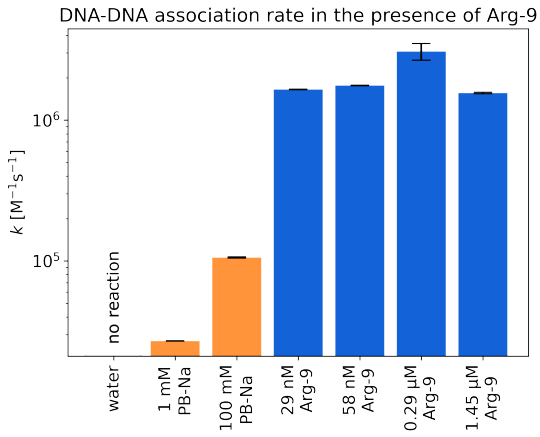

FIGURE 3.3: DNA-DNA association rate in PB-Na buffer and in the presence of Arg-9 introduced into 1 mM PB-Na buffer.

Having established the reaction acceleration by multicharged Arg-9, the potential catalytic effect of positively charged surfactants, including CTAC, CPC, and BTC, was investigated. Uncharged (Brij L23) and negatively charged (sodium dodecyl sulfate, SDS) served as controls.

These molecules can catalyze the reaction either as free surfactant molecules or as micelles, which form above the critical micelle concentration (CMC). Reaction rates were expected to vary depending on system composition. Therefore, the influence of surfactant concentrations on the hybridization rate was examined above and below the CMC under identical experimental conditions (1 mM PB-Na, 10 nM DNA-DNA). The concentrations of surfactants were 0.01 mM, 0.1 mM, 0.5 mM, at CMC, and CMC +1 mM. The CMC values of CTAC, CPC, and BTC were 1.06 mM, 0.9 mM, and 2.8 mM, respectively, while the aggregation numbers were 81, 98, and 65.[99–101]

All CTAC, CPC, and BTC significantly enhance DNA-DNA association rates compared to PB-Na alone (Figure 3.4). For instance, at 0.01 mM (below CMC), k values for CTAC, CPC, and BTC were 1.81×10^7, 2.02×10^7, and 8.92×10^6 $M^{-1}s^{-1}$, respectively, which are orders of magnitude higher

than those for 1 mM PB (1.93×10^4 $M^{-1}s^{-1}$) and 100 mM PB (4.64×10^5 $M^{-1}s^{-1}$). Even at higher concentrations near or above their CMC (e.g., 0.5 mM), the association rates remained high, with CTAC reaching 1.94×10^7, CPC at 1.16×10^7, and BTC at 4.30×10^6 $M^{-1}s^{-1}$.

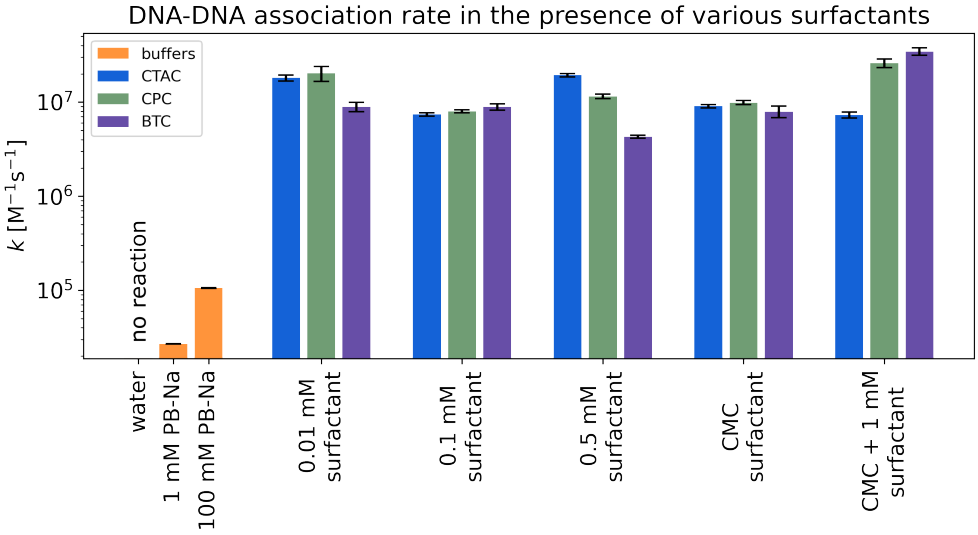

FIGURE 3.4: DNA-DNA association rate in PB-Na buffer and in the presence of various positive-charged surfactants introduced into 1 mM PB-Na buffer.

The mechanism behind this enhancement lies in the strong electrostatic attraction between the positively charged surfactant head groups and the negatively charged phosphate backbone of DNA, which reduces electrostatic repulsion and promotes closer DNA-DNA interactions. Studies have shown that cationic surfactants induce DNA condensation and aggregation by neutralizing DNA charges, facilitating its association.[102] However, the minimal variation in DNA association rates across different surfactant concentrations suggests that this process reaches saturation. Once DNA's negative charges are sufficiently neutralized, additional surfactant molecules do not further enhance the reaction. Additionally, a balance between hydrophobic and electrostatic interactions likely contributes to this saturation; excess surfactant may aggregate around DNA or induce steric hindrance, further limiting association rate increases. In contrast, nonionic surfactants such as Brij L23 and anionic surfactants such as SDS do not promote DNA-DNA association due

to their inability to neutralize DNA's negative charge (Figure 3.5). This aligns with findings that nonionic surfactants exhibit weak or negligible interactions with DNA, as their lack of charge prevents effective binding.[103]

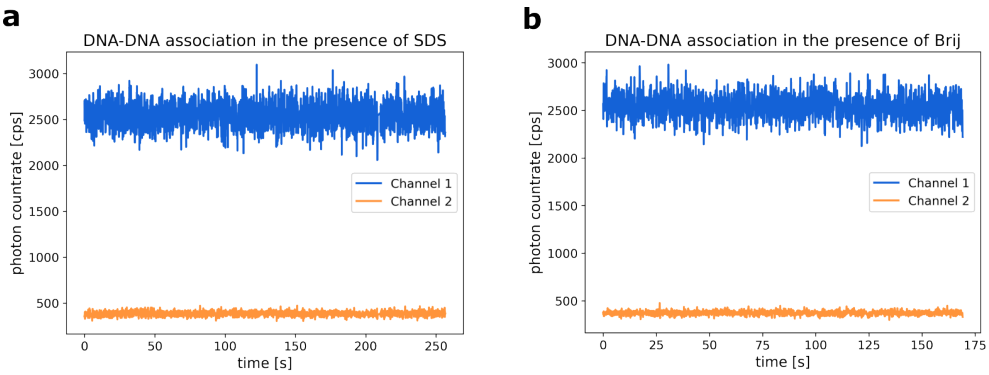

FIGURE 3.5: Fluorescence signals of DNAs recorded in the presence of **(a)** SDS and **(b)** Brij in water. Channel 1 shows the FRET donor signal, while channel 2 the FRET acceptor signal. No double-strand formation was observed in both SDS and Brij solutions.

3.1.4 Modeling DNA-DNA Association Rate in Relation to the Distribution of Charge on Catalyst

A theoretical model was developed to predict the acceleration of reactions between like-charged molecules in aqueous solutions facilitated by oppositely charged catalysts. The model was motivated by observing a similar acceleration in two experimental systems: DNA-DNA association (described in the previous sections) and covalent binding of two Coenzyme A (CoA) molecules (not considered in this thesis).[104]

The model predicts that catalytic enhancement arises primarily from increased reactant transport rather than specific molecular interactions. When the size of the catalyst is comparable to or larger than the Debye length (λ_D), its net charge becomes effectively screened in solution and is thus not sensed by localized probe charges. Instead, the surface charge density χ becomes the dominant factor influencing the system. Employing the Debye–Hückel approximation for a planar surface, the shift in electrostatic energy experienced by a reactant with charge q_r as it moves from the bulk to the catalyst surface is expressed by:

$$\kappa = \frac{q_r \chi \lambda_D}{2\pi\varepsilon_0 \varepsilon k_B T} \tag{3.3}$$

where ε_0 is the vacuum permittivity, ε the relative permittivity of water, k_B the Boltzmann constant, and T the temperature. This dimensionless parameter, scaled by the energy of thermal fluctuations, serves as a critical factor in describing the electrostatic interactions between the reactant and the catalyst.

Further, to quantify the transport-limited reaction rate, Smoluchowski's equation is utilized, linking the diffusive flux of particles from the bulk to the reactive catalyst surface. The resulting reaction rate constant k is directly influenced by κ leading to:

$$k = -k_0 \kappa, \tag{3.4}$$

where k_0 is an experimentally derived constant specific to the catalyst–reactant system. The negative sign ensures that greater attraction (more negative κ) corresponds to a higher reaction rate, such that k increases as κ becomes more negative. This linear dependency between k and κ is validated through experimental data, which show consistent proportionality when plotting k/k_0 against κ for both CoA and DNA systems (Figure 3.6).

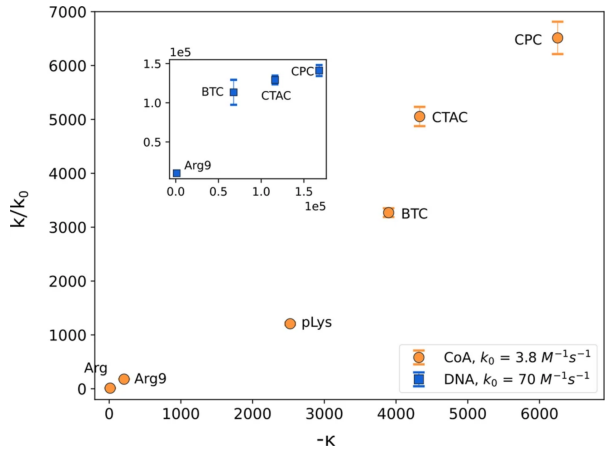

FIGURE 3.6: k/k_0 as a function of κ for CoA (orange dots) and DNA (blue dots) systems. The reaction rate increases with decreasing κ. The values of k_0 were determined by fitting the experimental data for each reactant to Equation 3.4. The alignment of data points exhibiting linear behavior indicates high model predictability.

3.2 DNA-DNA Interactions at Equilibrium

This section describes DNA-DNA interactions at equilibrium in the presence of monovalent cations and molecular crowders. The influence of ion-crowder interactions on nucleic acid hybridization is also addressed, followed by a phenomenological model describing the effects of molecular crowding.

3.2.1 Impact of Cations Concentration on DNA-DNA Interactions

To elucidate the interactions of nucleic acids in ionic solutions, the equilibrium constant of DNA-DNA duplex formation K was systematically measured as a function of sodium (Na^+) and potassium (K^+) ion concentrations. The cations were introduced in the form of phosphate buffer salts at pH 7.4 (PB-Na and PB-K), with concentrations ranging from 2 mM to 1 M. The experimental setup utilized 13-base pair oligonucleotides labeled with two fluorescent dyes (System 3, Section 2.1.1), maintaining a constant oligonucleotide concentration of 10 nM. Figure 3.7 illustrates K as a function of Na^+ and K^+ concentrations on a log-log scale.

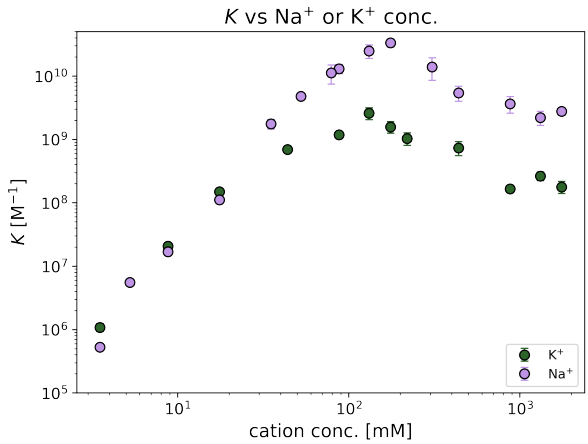

FIGURE 3.7: DNA-DNA equilibrium constant K in the presence of sodium (Na^+) and potassium (K^+) cation concentrations. Na^+ and K^+ were introduced as phosphate buffer salts, PB-K and PB-Na, respectively, at pH 7.4. The initial increase in K with rising concentrations of both Na^+ and K^+ results from the screening of the negative charges on DNA backbones by these cations, whereas the subsequent decrease in K is attributed to overscreening of the DNA backbone and ion crowding effects.

As the ionic concentration increased from 2 mM to approximately 150 mM, K exhibited a significant rise by three orders of magnitude for K^+ and four orders of magnitude for Na^+. This enhancement in duplex stability is attributed to the reduction in electrostatic repulsion between the negatively charged DNA strands. At higher ionic strengths, the increased charge screening over short distances stabilizes the DNA duplex by effectively neutralizing the phosphate backbone charges. These observations are consistent with the concept of the Debye length, which quantifies the effective range of electrostatic interactions in solution. As ion concentration increases, the Debye length decreases, leading to more efficient charge screening and stabilization of the DNA duplex.

However, beyond specific ion concentrations, a decrease in K was observed. For Na^+, this decline initiated at concentrations above approximately 170 mM, whereas for K^+, it occurred beyond 130 mM. This reduction in duplex stability at high ionic strength is not attributed to an increase in screening length, since the Debye length continues to decrease, but rather to ion crowding and overscreening effects. At these elevated concentrations, excess cations can overneutralize the DNA phosphate backbone, disrupting the electrostatic balance required for stable duplex formation.[105] In addition, the high local ion density may perturb hydration shells and reduce DNA flexibility, further contributing to destabilization.

Notably, Na^+ consistently stabilizes DNA duplex formation more effectively than K^+ at equivalent concentrations. For instance, the maximum K values observed were $\sim 4 \cdot 10^{10}$ for Na^+ and $\sim 2 \cdot 10^{9}$ for K^+, representing more than an order of magnitude difference. This trend persists for cation concentrations $>\sim$50 mM, with Na^+ achieving significantly higher K values compared to K^+. The higher stabilizing effect of Na^+ is attributed to its smaller ionic radius, which facilitates more effective charge neutralization and closer interaction with the DNA phosphate backbone. In contrast, K^+, with its larger ionic radius and weaker hydration shell, provides less effective stabilization.[106]

3.2.2 DNA-DNA Duplex Stability in Crowded Environment

Refractive Index Correction

The addition of molecular crowders alters the refractive index of the solution, which in turn affects the confocal volume used in fluorescence-based measurements. To account for this optical effect, the refractive indexes of crowder solutions at varying concentrations were first measured (Figure 3.8). The confocal volumes corresponding to each solution were then corrected by multiplying by the factor $RI_c/RI_{PB\text{-}Na}$, where RI_c represents the refractive index of the crowder-containing solution, and $RI_{PB\text{-}Na}$ is the reference index of the PB-Na buffer.

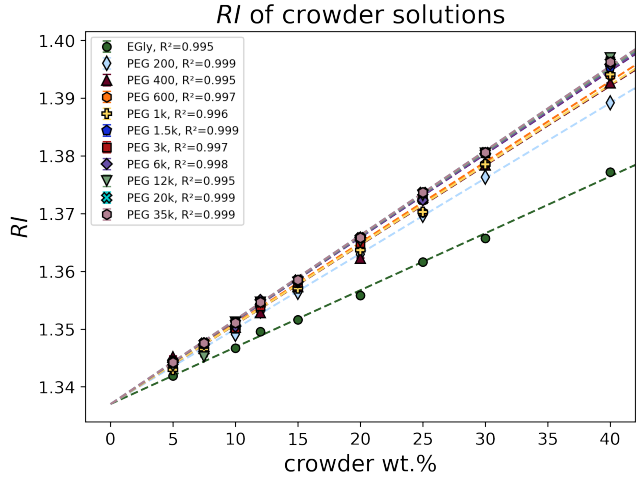

FIGURE 3.8: Refractive indexes (RI) of PEG solutions at various crowder concentrations with linear fits (dashed lines).

Hybridization Kinetics in Crowded Environments

Molecular crowders also influence the kinetics of DNA strand association by slowing hybridization rates. To assess this effect, hybridization kinetics were measured in the presence of the lowest and highest molecular weight crowders – ethylene glycol (EG) and polyethylene glycol (PEG) 35k – each at 40 wt.% (Figure 3.9). At this concentration, the half-time for duplex formation was approximately 2 hours for EG and 4 hours for PEG 35k. Therefore, to

ensure equilibrium was reached under all conditions, an incubation period of 48 hours was used in subsequent experiments.

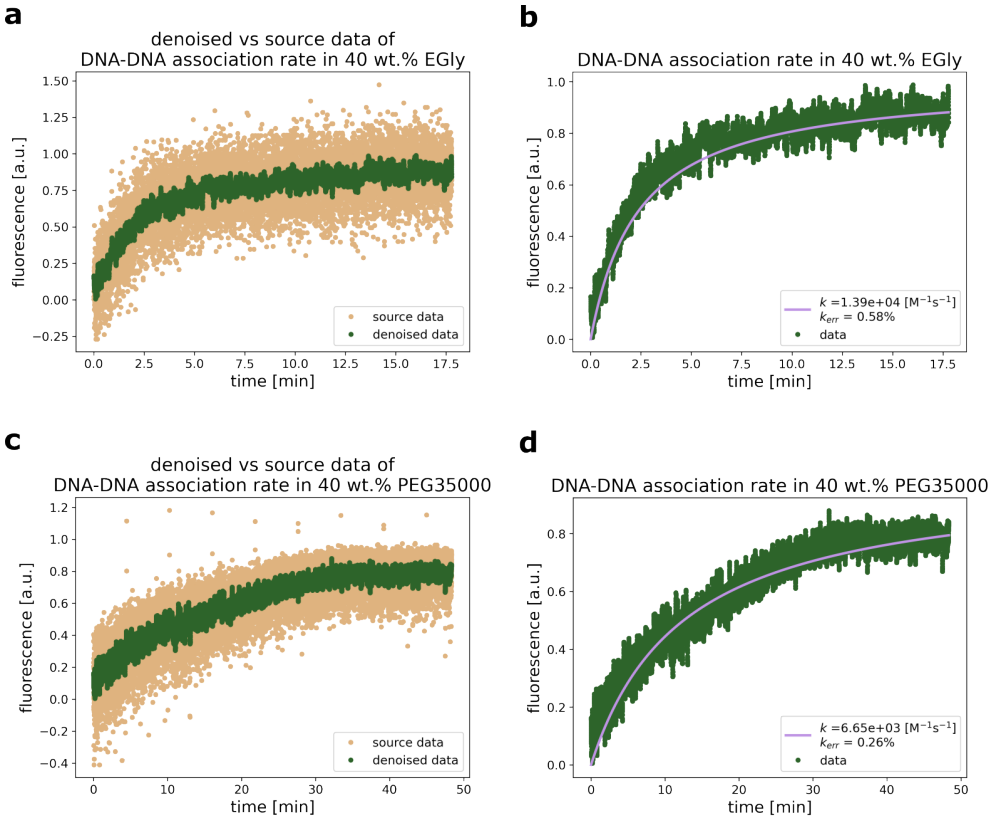

FIGURE 3.9: DNA-DNA association rates in **(b)** 40 wt.% ethylene glycol and **(d)** 40 wt.% PEG 35k. Panels **(a)** and **(c)** show raw and filtered data, respectively, processed using the Savitzky–Golay filter with a window size of 37 and a cubic polynomial.[107] Rate constants were determined as described in Section 3.1.

Thermodynamic Analysis of DNA Hybridization

The thermodynamic consequences of molecular crowding on DNA-DNA interactions were systematically studied using EG and PEGs ranging from 200 to 35,000 Da. The equilibrium constant (K) and standard Gibbs free energy change (ΔG) were quantified across varying concentrations of each crowder, where ΔG represents the shift between K measured at specific crowder concentration vs K measured in buffer solution – K_0

Hybridization experiments were performed using dual-labeled 13-base-pair-long oligonucleotides at a constant DNA concentration of 10 nM in 20 mM PB-Na buffer supplemented with 0.002% Tween 20. DNA concentration, buffer composition, and surfactant content were held constant while different amounts of crowders were added, followed by thorough mixing and incubation.

Figure 3.10 summarizes how K and ΔG vary with crowder concentration. Two distinct trends were observed: (i) For small crowders (e.g., EG, PEG 200), K decreased monotonically by up to three orders of magnitude. (ii) For larger crowders (PEGs > 600 Da), K initially increased – typically peaking between 5 wt.% and 20 wt.% – before declining significantly at higher concentrations.

In EG, K decreased from $2 \cdot 10^9$ M^{-1} (buffer) to $5 \cdot 10^6$ M^{-1} (40 wt.%), with ΔG increasing by approximately +14.9 kJ/mol. This destabilization is attributed to EG–DNA interactions that influence solvation and weaken base pairing. Unlike larger crowders that exclude volume, EG freely diffuses into the DNA's hydration shell and interacts with phosphate groups through hydrogen bonding.[108] These interactions interfere with duplex formation by disrupting solvation and base pairing.[109]

In contrast, PEG 6k induced a biphasic response. K increased from $2 \cdot 10^9$ M^{-1} in buffer to $3 \cdot 10^{10}$ M^{-1} at 12.5 wt.%, then declined to 10^9 M^{-1} at 40 wt.%. ΔG decreased by -6.71 kJ/mol at 12.5 wt.%, then increased by +1.72 kJ/mol at 40 wt.%. The initial stabilization is consistent with depletion interactions: PEGs are sterically excluded from the space between DNA molecules, creating osmotic pressure that promotes hybridization. However, at higher concentrations crowding-induced destabilization reduces number of complexed DNAs. Additionally, PEGs can bind Na^+ ions, altering the ionic environment.[14] This reduces screening of the negatively charged DNA backbones, enhancing repulsion and further modulating hybridization efficiency.

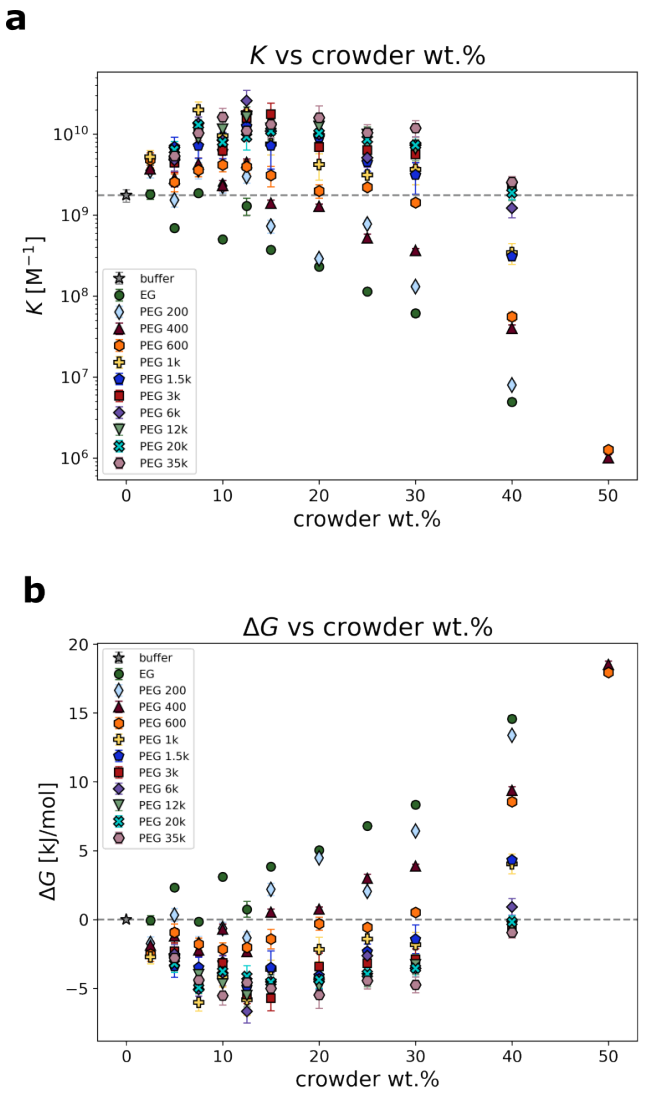

FIGURE 3.10: **(a)** Equilibrium constant (K) and **(b)** Gibbs free energy (ΔG) of DNA-DNA hybridization as a function of EG and PEG concentrations. ΔG was calculated using Equation 1.3 ($R = 8.314\ \mathrm{J{\cdot}mol^{-1}{\cdot}K^{-1}}$, $T = 298$ K) from the measured K values, normalized to those in buffer K_0.

Phenomenological Modeling of Crowding Effects

To describe the non-monotonic dependence of crowders on DNA-DNA hybridization, a phenomenological equation (Molecular Crowding fit, MC fit) was introduced in which the natural logarithm of K is expressed as a quadratic function of crowder concentration c_{crowder}:

$$\ln(K) = a_0 + a_1 c_{\text{crowder}} + a_2 c_{\text{crowder}}^2. \tag{3.5}$$

This simple quadratic form effectively captures the biphasic behavior observed experimentally: an initial increase in K at low crowder concentrations, followed by a decrease at higher concentrations. The linear term (a_1) reflects stabilizing effects arising from depletion forces and excluded volume interactions, which enhance hybridization. In contrast, the quadratic term (a_2), typically negative, accounts for destabilizing contributions such as elevated viscosity, restricted molecular diffusion, altered electrostatic screening due to ion redistribution, and disruption of the DNA hydration shell.[109] The model thus offers a compact yet mechanistically interpretable framework for describing the interplay between opposing crowding effects.

Figure 3.11 shows Molecular Crowding fits, while Figure 3.12 presents the fitted coefficients a_0, a_1, and a_2, illustrating the ability of the quadratic equation to reproduce both monotonic and non-monotonic trends. The intercept a_0 remained constant, consistent with K_0 measured in the absence of crowders. In contrast, both a_1 and a_2 exhibited systematic dependence on the crowder molecular weight and monomer number. In agreement with theoretical and simulation studies,[51] larger crowders tended to produce more positive a_1 values – indicating stronger depletion-driven stabilization – while simultaneously exhibiting more negative a_2 values, reflecting enhanced destabilization at high concentrations due to physical confinement and electrostatic effects.

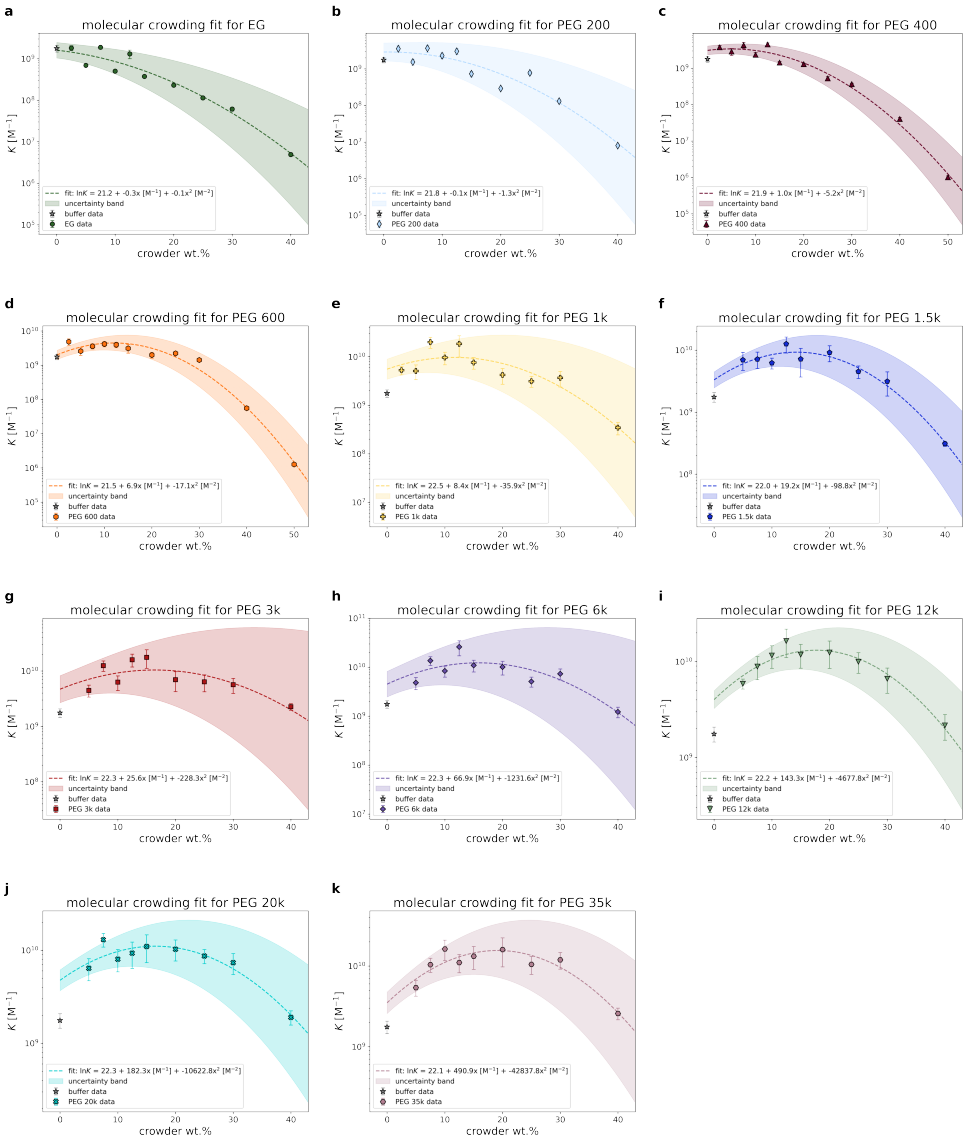

FIGURE 3.11: Molecular Crowding fits for all measured crowders. Dashed lines represent model fits of K values obtained using Equation 3.5, with coefficients a0, a1, and a2 corresponding to the intercept, linear, and quadratic terms, respectively. Shaded areas indicate the uncertainty bands associated with each fit.

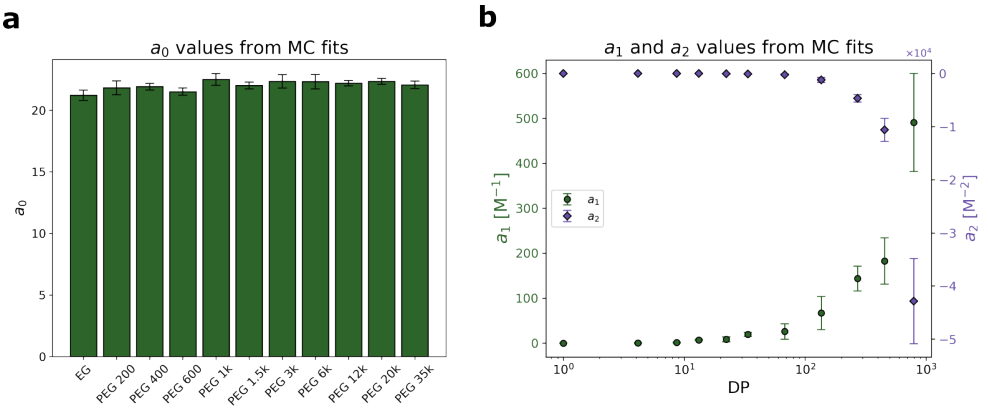

FIGURE 3.12: Fitted a_0, a_1, and a_2 coefficients for all studied crowders. The coefficients a_0, a_1, and a_2 were derived using Equation 3.5 and correspond to intercept, linear, and quadratic terms of the Molecular Crowding fit, respectively. DP in plot **(b)** denotes degree of polymerization.

While the current model remains phenomenological, it highlights that molecular crowding is not a singular effect but rather an emergent outcome of multiple competing interactions, including steric exclusion, solvation dynamics, and electrostatics. The fitted parameters a_1 and a_2 serve as effective proxies for these opposing contributions and enable a comparative analysis across different crowding conditions. However, the model does not explicitly resolve the mechanistic origin of these effects. Future extensions could incorporate specific interactions, such as sodium ion complexation by PEG, which lowers ionic strength and modulates electrostatic repulsion between DNA backbones. This contribution can be described analytically using complexation equilibria and Debye–Hückel theory. Likewise, depletion interactions could be treated more rigorously via the Asakura–Oosawa model,[110] linking crowding-induced stabilization to osmotic pressure and exclusion volume. Although such refinements lie beyond the scope of this work, they offer a promising direction for developing more predictive, mechanistically grounded models of crowding effects on nucleic acid hybridization.

3.3 Microfluidic-Based Platform for Semi-Automated Measurement of Biomolecule Interactions

This section presents the development and operation of a microfluidic-based platform for semi-automated measurements of biomolecule interactions, founded on the DNA-DNA hybridization example. Additionally, it describes the platform's validation, assesses its capabilities, and compares its throughput to that of the standard method.

3.3.1 Fundamentals of System Operation

The experimental setup comprises three integrated units: the Droplet On-Demand Unit (DODU), the Detection Unit (DU), and the Computation Unit (CU), illustrated in Figure 3.13. The DODU is designed to produce droplets with precise volumes and defined reactant concentrations. The DU immobilizes droplets at specific locations for fluorescence signal detection, while the CU coordinates the dilution process, adjusts reactant flow based on real-time camera feedback, and processes experimental data.

At the center of the DODU is a microfluidic device capable of adjusting droplet concentrations by merging and splitting operations. Fundamental droplet manipulations are achieved through specialized microfluidic traps integrated into the flow channels. These traps alter droplet motion using bypass slits and localized channel constrictions. By modifying their geometric dimensions, a range of functionalities is implemented, as shown previously.[111] This study employs two distinct trap designs: metering traps (Figure 3.14a, top left panel) and merging traps (Figure 3.14a, top right panel), for precise concentration control.

Metering traps include a single obstacle, which influences droplets based on flow direction. Droplets approaching from the side with the obstacle remain unaffected, while those moving in the reverse direction are immobilized if their size is smaller than the trap or divided into two segments if they exceed the trap size. One segment corresponds to the trap's defined volume, while the excess continues downstream. Reversing the flow allows the immobilized portion to be released. The droplet formation process is depicted

in Figure 3.14b. During the initial flow phases (t_1 and t_2), the liquid passes downstream; reversing the flow (t_3, t_4) shapes the droplet according to the trap geometry. A subsequent reversal (t_5) releases the droplet, resulting in either uniform droplets or the division of double-sized droplets into equal parts.

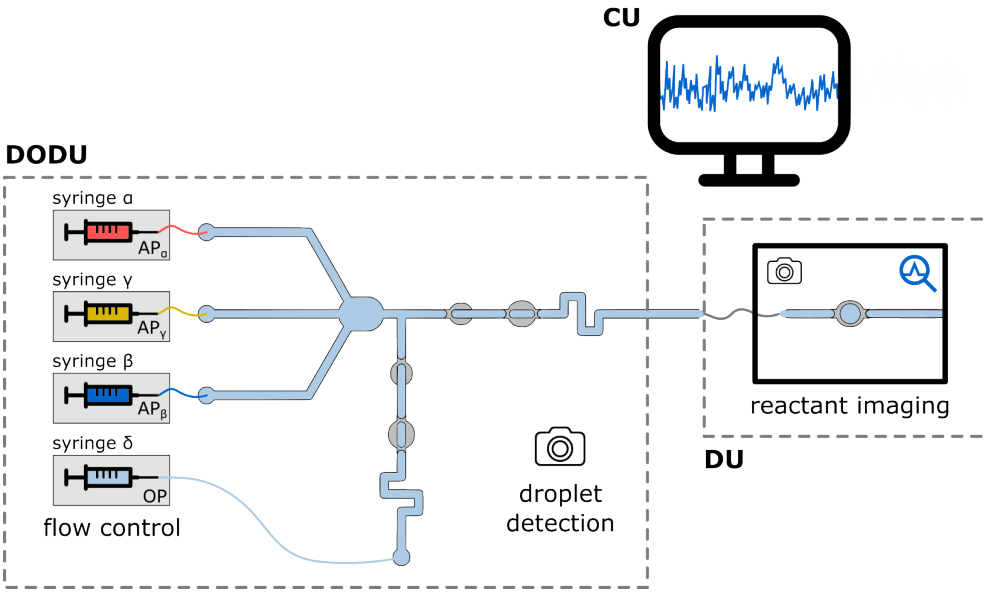

FIGURE 3.13: Schematic representation of the microfluidic-based platform, comprising the Droplet On Demand Unit (DODU), Detection Unit (DU), and Computation Unit (CU). The DODU consists of four syringe pumps – three for the aqueous phases (AP_α, AP_β, AP_γ) and one for the oil phase (OP) – a microfluidic chip featuring metering and merging traps, and a camera unit for real-time monitoring and control of liquid flows. According to the programmed protocol, the DODU enables droplet generation, merging, and splitting, after which the droplets are transported to the DU via tubing. The DU includes a detection trap and a camera unit for real-time monitoring of droplet position, and is integrated with a confocal microscope. The CU orchestrates the dilution process and dynamically adjusts the flow rates of reactants.

In contrast, merging traps immobilize smaller droplets regardless of flow direction while allowing larger droplets to pass freely. The merging trap's function differs from the metering trap due to variations in bypass slit geometry and liquid flow rates. When two droplets encounter each other in a merging trap, their behavior depends on the presence of an electromagnetic

field (EMF). Without EMF, coalescence is hindered by interfacial tension and the thin oil film separating the droplets. Applying EMF alters the charge distribution at the water/oil interface, reducing the energy barrier and enabling droplet fusion. Once merged, the droplet exits the trap due to its increased size, as shown in Figure 3.14c. This system utilizes explicitly merging traps to combine two unit-sized droplets into a single double-sized droplet with mixed contents.

Double-sized droplets are transported from the DODU to the DU through detachable tubing. This connection allows for droplet storage, which is essential for equilibration, although, in this study, tubing primarily serves as a transport medium, given the rapid stabilization of DNA double-stranded complexes in phosphate buffers as shown in Section 3.1.2.

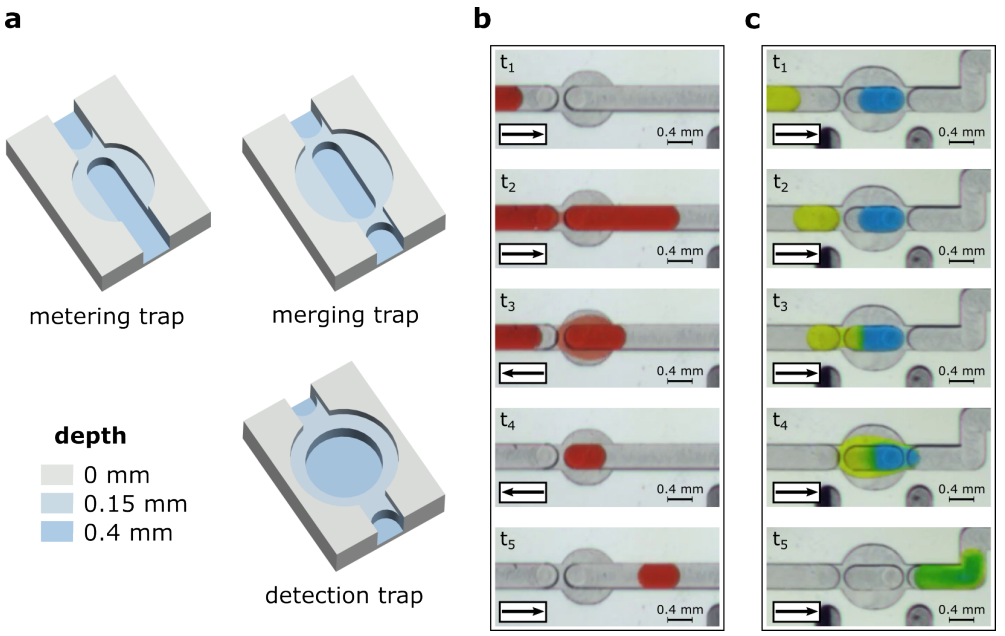

FIGURE 3.14: Hydrodynamic traps and their functioning. **(a)** Detailed geometries of the hydrodynamic traps used in the cores of the DODU and DU (top left — metering trap, top right — merging trap, bottom right — detection trap), with depth variations represented by different colors. **(b, c)** Experimental images captured at different instances ($t_1 - t_5$), demonstrating the operation of **(c)** the metering trap and **(d)** the merging trap. Arrows denote the directions of oil flow.

The DU consists of a microfluidic chip, a camera, and a confocal microscope configured for FCS. The chip features a single channel with a detection trap centrally positioned and connected to a waste reservoir at the outlet. Unlike the metering and merging traps, the detection trap has a unique geometry tailored for FCS measurements, as shown in Figure 3.14a, bottom right panel. The detection trap immobilizes smaller droplets while permitting larger ones to pass, simultaneously providing a sufficient surface area for focal volume alignment.

The DODU incorporates a microfluidic core, four bidirectional syringe pumps (α, β, γ, δ), and a camera for real-time droplet monitoring. The core includes two channels – Channel 1 and Channel 2 – each featuring metering and merging traps in sequence. In this system, the mixing and droplet manipulation steps are distributed across both channels for improved efficiency and control.[112] The microfluidic core has three aqueous phase inlets (AP_α, AP_β, AP_γ), a dispensation chamber, and two outlets. While both channels share a similar arrangement, Channel 1 connects to the DU, and Channel 2 links to the oil phase (OP) pump. Metering traps are positioned such that droplets form only during flow reversal, and merging traps are separated by short canals to avoid unintentional droplet formation. Detailed schematics of the DODU and DU cores are presented in Section 2.2.2, Figure 2.3.

To determine K using the MBA approach, a reactant at a fixed concentration is mixed with serial dilutions of a second reactant. Therefore, Channel 1 was utilized for diluting AP_β with AP_γ at specific ratios, while Channel 2 mixed AP_α with diluted AP_β droplets. Real-time imaging data processed by the CU controlled the flow of reactants to the appropriate locations. In the DODU core, the workflow proceeded as follows: Syringe α dispensed AP_α into Channel 1 (Figure 3.15a. After passing Metering Trap 1, the flow reversed, creating an AP_α droplet (Figure 3.15b). Syringe δ then introduced oil, moving the droplet to Merging Trap 1 (Figure 3.15c). To prevent timing discrepancies between system feedback and liquid positions, the flow of AP_α was reversed before entering the merging trap. Similarly, Syringe β dispensed AP_β, which was pushed into Channel 2, while Syringe δ aspirated OP to guide the AP_β droplet through Metering Trap 2 (Figures 3.15d-e). This procedure repeated for AP_γ (Figures 3.15g-i).

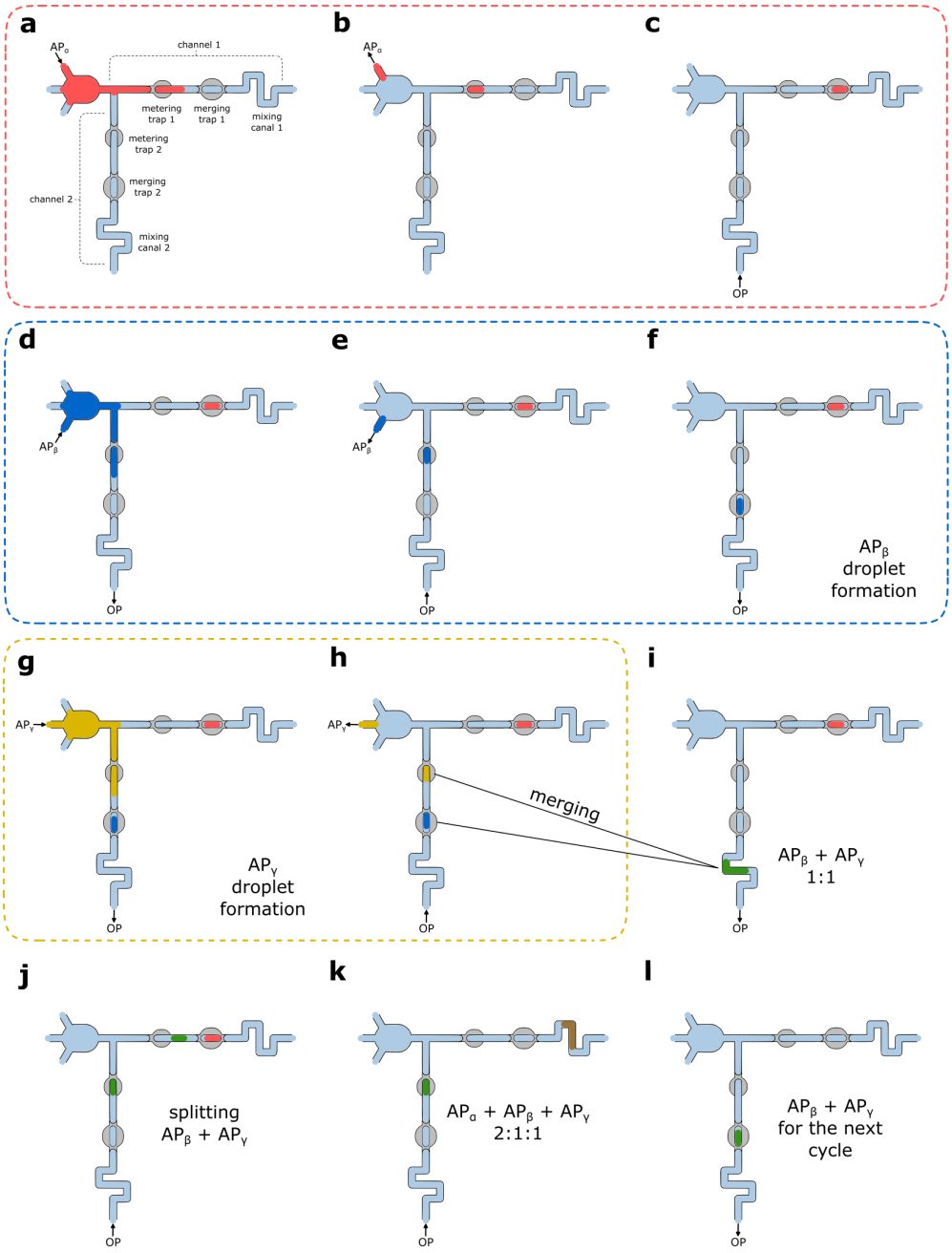

FIGURE 3.15: Flow operations during a single dilution cycle. **(a–c)** Formation of the AP_{α} droplet. **(d–i)** Sequential formation, mixing, and splitting of AP_{β} and AP_{γ} droplets. **(j–l)** Merging of AP_{α} with a mixture of AP_{β} and AP_{γ} in a 2:1:1 ratio. Arrows indicate the flow directions of the aqueous (AP) and oil (OP) phases at each stage of the cycle. **(a)** Defines the notation used throughout the article.

Once AP_γ reached Merging Trap 2, it coalesced with the AP_β droplet, and the combined droplet traversed the mixing canal. After mixing, Syringe β reversed the flow, splitting the droplet into two equal parts at Metering Trap 2 (Figure 3.15j). One portion merged with AP_α to form a mixture in a 2:1:1 ratio (AP_α:AP_β:AP_γ), which proceeded to the DU (Figure 3.15k), while the other returned to Merging Trap 2 for further processing (Figure 3.15l). This cycle, lasting approximately one minute per iteration, enabled precise droplet composition adjustments.

3.3.2 Validation of the System via Image-Based Droplet Analysis

System validation was performed by generating a series of 22 double-sized droplets using three food dyes introduced as aqueous phases: AP_α (red, 0.01 % Allura Red), AP_β (blue, 0.1 % Brilliant Blue), and AP_γ (yellow, 0.1 % Quinoline Yellow). Each droplet was designed such that AP_α contributed consistently to half of the total volume, while AP_β and AP_γ were mixed in varying ratios. The sequencing of AP_β and AP_γ blends is illustrated in Figure 3.16.

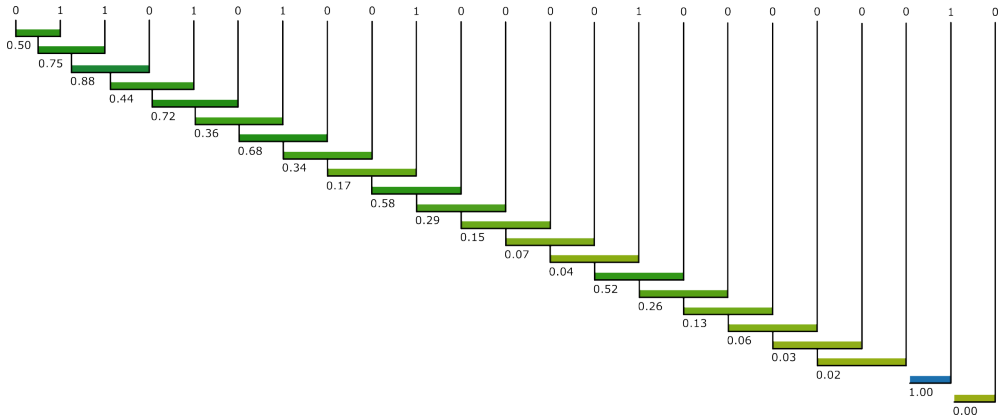

FIGURE 3.16: The droplet dilution sequence performed in this study. The binary values (0 and 1) at the top of the figure indicate the initial concentrations of dyes in the droplets, where 0 corresponds to yellow and 1 to blue. The concentration ratios resulting from mixing are shown along the horizontal lines. At each iteration, a droplet with the newly established ratio is merged with either a pure yellow or a pure blue droplet to achieve the desired sequence of dilutions.

To assess the reproducibility of the platform, individual frames from a video showcasing a full dilution process were analyzed to extract droplet contours at Metering Traps 1 and 2. Droplet volumes were calculated based on these contours, as shown in Figure 3.17. The methodology for volume estimation assumes droplets to be shaped as a cylinder with two hemispherical ends. The radius of the cylinder and spheres was set as half the channel width (0.2 mm), while the cylinder height, H_{cylinder}, was determined by repeatedly measuring the length of the droplet's contact with the channel. The detailed results are provided in Table 3.1. Using this approach, the average droplet volume was determined to be 97.62 ± 0.30 nL at Metering Trap 1 and 97.68 ± 0.27 nL at Metering Trap 2. Errors in volume measurements represent weighted means derived from the data in Table 3.1. These findings display exceptional reproducibility of the metering traps, with high consistency in droplet volumes across both traps.

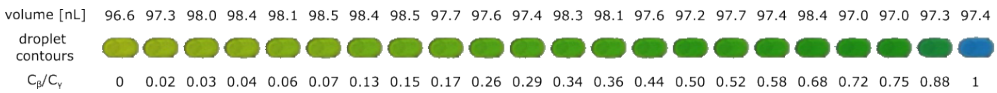

FIGURE 3.17: Validation of the dilution protocol and droplet volumes was conducted by analyzing images of droplets captured at Metering Trap 2. These snapshots illustrate the progressive increase in AP_β content within the droplets and the measured droplet volumes.

3.3.3 Measurements of DNA Concentration and Diffusion Coefficient in Droplets

The functionality of the microfluidic platform was further evaluated by modifying the aqueous phases (APs) and applying the system in confocal microscopy. AP_β and AP_γ was replaced with 20 mM PBS containing 0.01% Allura Red food dye to enhance visual contrast and 0.002% Tween 20 to prevent the accumulation of DNA strands at water/glass interface in the syringe pumps. AP_α contained the same buffer but included a single-stranded 20-base-pair-long DNA oligonucleotide labeled with a fluorescent dye.

The introduction of food dye resulted in minimal background noise (Figure 3.18a) as most photons emitted by the dye were reflected, minimizing potential errors during platform validation. The spectral characteristics of the

red food dye are presented in Figure 3.18b. Additionally, the food dye slightly increased the diffusion coefficient of DNA, D_{DNA}, from 127.00 ± 2.16 μm^2/s to 136.33 ± 1.25 μm^2/s, while the DNA concentration, C_{DNA}, remained unaffected (Figures 3.18c,d). The increase in D_{DNA} is probably due to DNA-dye interactions or a minor change in the refractive index of the solution, which affects the focal volume size.

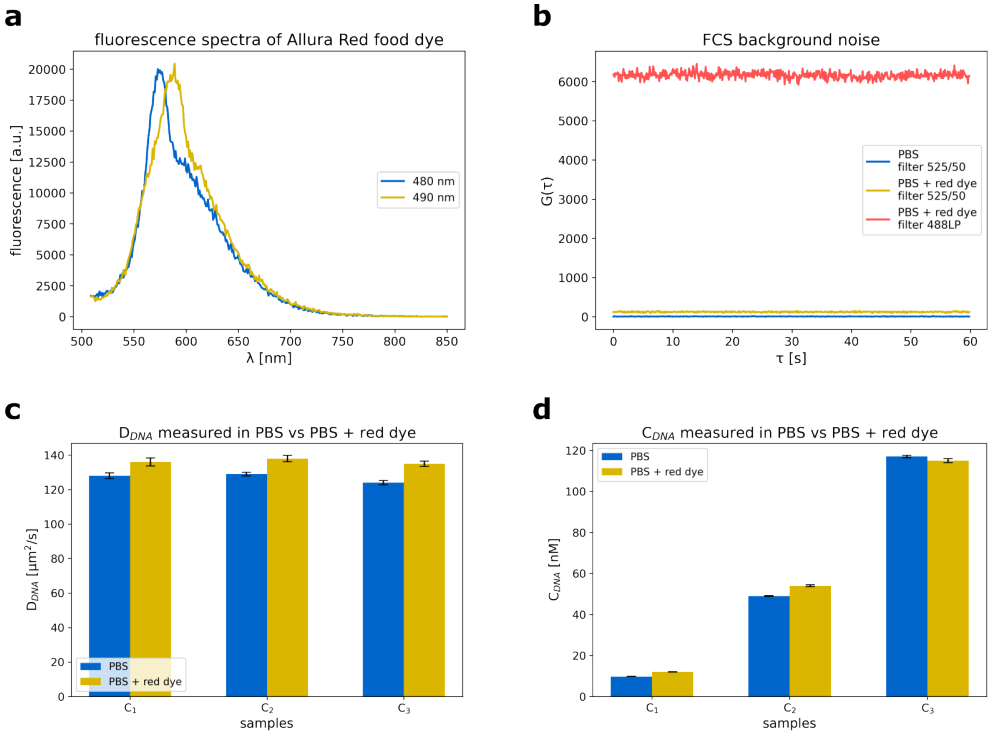

FIGURE 3.18: **(a)** Fluorescence spectra of 0.002% Allura Red food dye recorded following excitation at 480 nm and 490 nm. **(b)** To minimize background noise in Channel 1, a filter transmitting photons within the 500–550 nm wavelength range (525/50) was applied. For comparison, background noise was also measured using a long-pass filter that transmits photons with wavelengths greater than 485 nm (485LP). **(c,d)** Bar plots summarizing the measured DNA concentrations and diffusion coefficients in PBS and PBS with 0.01% Allura Red food dye.

To assess whether DNA remained in the aqueous phase without interacting with the surfactant at the PBS/oil interface, a single droplet was generated and immersed in oil containing fluorinated surfactant. Fluorescence intensity

fluctuations of diffusing DNA molecules were monitored within a focal volume positioned inside a droplet immobilized in the detection trap. Using the autocorrelation function, intensity fluctuations over time, $f(t)$, were compared with those after a lag time, $f(t+\tau)$, to determine C_{DNA} and D_{DNA}. Figure 3.19a presents an example of the autocorrelation function fitted to the fluorescence signal of DNA within a droplet. The concentration, C_{DNA}, and diffusion coefficient, D_{DNA}, were monitored over five hours. Figure 3.19b depicts the reactant concentration inside the droplet, while Figure 3.19d presents the corresponding diffusion coefficient. The stability of C_{DNA} over time confirms that DNA concentration remained unchanged within the droplet, while the constant value of D_{DNA} indicates the structural stability of the reactant. Using the average diffusion coefficient, the DNA hydrodynamic radius was calculated via the Stokes-Einstein equation, yielding 1.71 ± 0.05 nm. This value closely matched the control measurement (1.74 ± 0.02 nm) obtained from a droplet that had no contact with the oil phase. The consistency in hydrodynamic size confirms the absence of complex formation between DNA and the uncharged surfactant at the water/oil interface – a similar behavior to Brij L23 (Section 3.1.3).

Although the analysis of tinted droplets provided insights into droplet morphology, dye dispersion, and overall system functionality, it did not directly reveal the biomolecule concentration profile across serial dilutions. To address this, additional validation of system performance was conducted. The dilution protocol was repeated under the same conditions as in previous measurements, and the actual DNA concentration in droplets was plotted against the expected values (Figure 3.19d). The results demonstrated an excellent correlation between predicted and measured concentrations (R^2 = 0.994), confirming the high accuracy of the dilution process. Furthermore, the data indicate that reactant concentrations were evenly distributed across droplets following mixing without being affected by droplet movement.

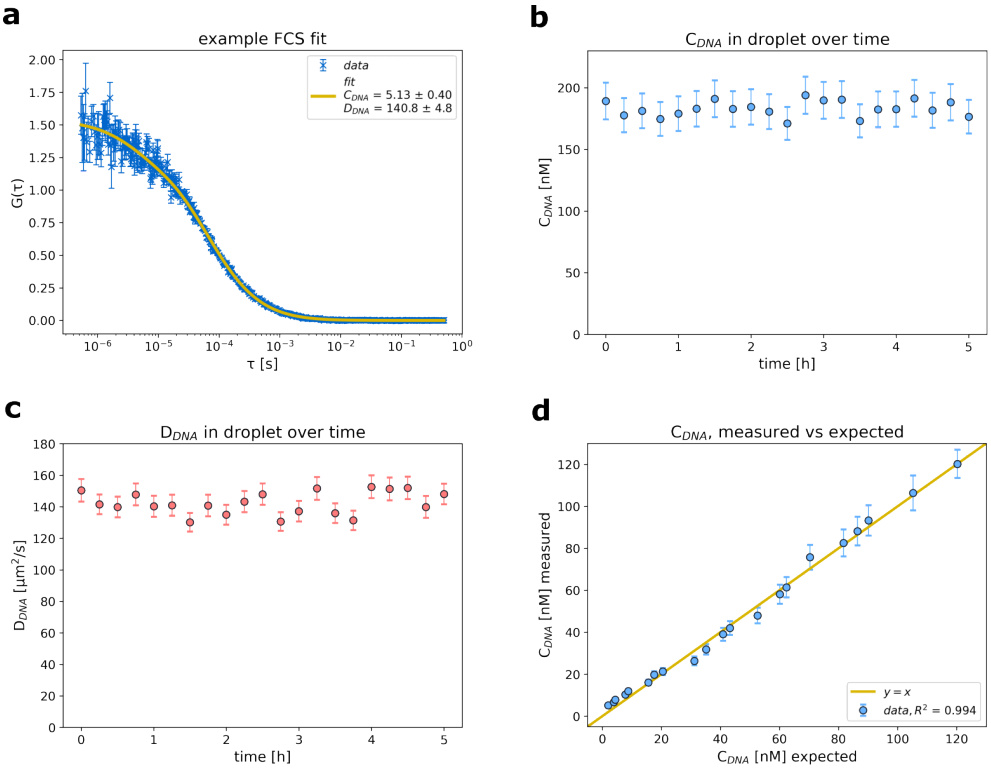

FIGURE 3.19: **(a)** An example of an individual FCS measurement within a nanoliter droplet, where τ represents the lag time and $G(\tau)$ denotes the autocorrelation function of fluorescence intensity fluctuations. **(b)** Stability of DNA concentration over time within a single droplet immobilized in the detection trap. **(c)** Temporal consistency of the DNA diffusion coefficient within the same droplet. **(d)** Comparison between expected and experimentally determined DNA concentrations in droplets, validating the accuracy of the dilution process performed by the platform.

3.3.4 Platform Application to Study DNA-DNA Interactions

To assess the platform's performance, the equilibrium constant for DNA-DNA double-strand complex formation ($K_{DNA-DNA}$) was determined by labeling both reactants with fluorescent dyes and monitoring FRET. Oligonucleotides were introduced into 20 mM PBS containing 0.01% red food dye to enhance the visibility of droplets against the oil phase. In this setup, AP_{α} acted as the energy donor, AP_{β} as the energy acceptor, and AP_{γ} as the diluting phase. The donor concentration in droplets was maintained at

10 nM, while the acceptor concentration varied from 0 to 100 nM. Before entering the detection unit, the droplets underwent a complete dilution sequence, allowing sufficient time for the reactants to reach equilibrium.

The equilibrium constant measured in droplets formed by the platform was 3.1×10^8 $M^{-1} \pm 5.5\%$ (Figure 3.20a, red dashed line), which was in close agreement with the value obtained through the standard procedure, 2.8×10^8 $M^{-1} \pm 7.0\%$ (Figure 3.20a, blue continuous line). Uncertainties in $K_{DNA-DNA}$ were determined using the least-squares fitting method, while variations in the countrate were attributed to instrumental limitations and sample preparation inconsistencies.

To showcase the capabilities of the platform, DNA-DNA interactions were investigated as a function of ionic strength (I). The fluorescent acceptor was substituted with a non-fluorescent analog. Under these conditions, the brightness change of the labeled strand during hybridization with its complementary sequence was no longer influenced by FRET. To minimize background noise that could interfere with the measurements, the food dye was removed from the solution.

Ionic strength variations were introduced by preparing PBS solutions at different concentrations (5 mM, 10 mM, 20 mM, 30 mM, 50 mM, 75 mM, 100 mM, 125 mM, and 150 mM) and were determined using the equation:

$$I = \frac{1}{2} \sum_{i=1}^{n} c_i z_i^2, \tag{3.6}$$

where c_i is the concentration of ion i, and z_i represents its charge number. The relationship between $K_{DNA-DNA}$ and I is depicted in Figure 3.20b, with error bars reflecting uncertainties obtained from the least-squares fitting approach. Similarly, as for PB-Na and PB-K buffers (Section 3.2.1), an increase in ionic strength led to a higher $K_{DNA-DNA}$, which can be attributed to a reduction in electrostatic repulsion between negatively charged DNA strands.

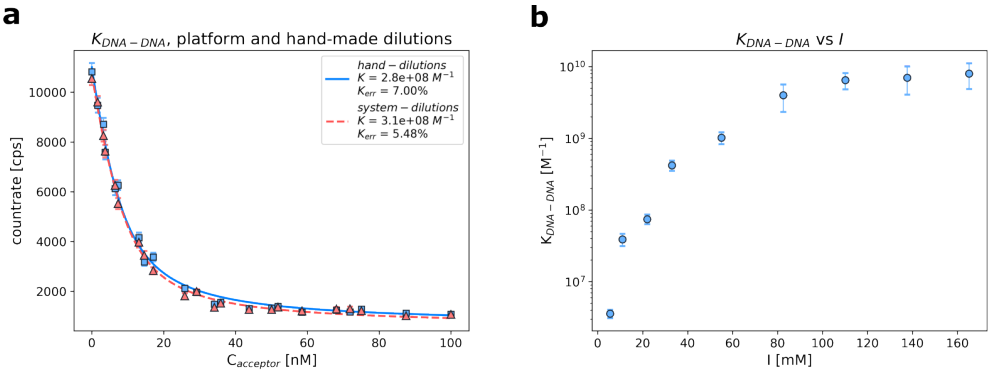

FIGURE 3.20: **(a)** The comparison of the equilibrium constant of the DNA-DNA association reaction prepared by hand-made dilutions (blue line) and by the platform (red dashed line). **(b)** DNA-DNA equilibrium constant ($K_{DNA-DNA}$) as a function of ionic strengths (I). I was consecutively increased by varying the sodium phosphate buffer at pH 7.4.

3.3.5 Manual vs. Automated Workflows

The determination of a single equilibrium constant (K) in a given solution follows a standardized protocol comprising several sequential steps: (i) calibration of the confocal microscope, (ii) preparation of stock solutions, (iii) execution of serial dilutions, (iv) mixing of samples, (v) transfer of solutions to confocal microscopy-compatible plates, (vi) acquisition of measurements, and (vii) data analysis. Steps (iii) and (iv), when applied to 20 samples, typically necessitate approximately one hour of manual labor. Similarly, steps (v) and (vi) require roughly two hours, during which the operator manually adjusts the microscope stage along the x, y, and z axes to position the focal volume within each sample and initiates the measurement process. This procedure is repeated 20 times to obtain individual measurements.

The implementation of an automated system has streamlined steps (iii) through (vi), substantially reducing the operator's workload. Specifically, the automation of these steps saves approximately three hours of operator time per single K value determination. For more intricate investigations, such as one described in Section 3.3.4, the system conserved $\sim$27 hours (for nine K value measurements). Concurrently, the automated system completed these

measurements in ∼5.5 hours. The observed discrepancy between the operator time saved and the total measurement duration of the automated system can be attributed to several factors. These include the elimination of manual focal volume adjustments between plate wells, the removal of plate exchange steps, and the reduction in sample dilution time. This automation not only enhances operational efficiency but also minimizes the likelihood of human error during repetitive tasks, thereby improving the reliability of the measurement process.

Furthermore, the conventional protocol relies on disposable 8-well plates, each requiring 200 μL of solution per well. This approach generates significant waste and incurs substantial costs, as a single plate ranges from $4 to $16 net, depending on the manufacturer and the type of glass substrate. In contrast, the proposed platform employs a reusable detection unit that utilizes nanoliter droplets separated by oil, reducing reagent consumption by a factor of 2000 and eliminating plate-related expenses. For instance, the 180 measurements conducted in Section 3.3.4 would cost approximately $230 using conventional plates, whereas the automated system incurs no such costs. This approach offers a more sustainable and economically viable alternative.

	Metering Trap 1				Metering Trap 2			
No.	$H_{cylinder}$ [mm]	H_{err} [mm]	V [nl]	V_{err} [nl]	$H_{cylinder}$ [mm]	H_{err} [mm]	V [nl]	V_{err} [nl]
1	0.506	0.011	97.093	1.375	0.502	0.007	96.627	0.885
2	0.511	0.009	97.722	1.098	0.508	0.010	97.327	1.310
3	0.505	0.014	96.914	1.712	0.514	0.011	98.045	1.351
4	0.520	0.012	98.853	1.470	0.516	0.012	98.368	1.570
5	0.515	0.013	98.242	1.589	0.514	0.010	98.099	1.258
6	0.514	0.014	98.134	1.770	0.517	0.009	98.529	1.153
7	0.503	0.014	96.752	1.768	0.516	0.015	98.404	1.828
8	0.514	0.014	98.152	1.813	0.517	0.013	98.529	1.641
9	0.518	0.010	98.637	1.212	0.511	0.009	97.686	1.143
10	0.512	0.008	97.901	1.051	0.510	0.004	97.596	0.498
11	0.494	0.011	95.603	1.376	0.509	0.011	97.434	1.368
12	0.513	0.012	97.955	1.472	0.515	0.009	98.278	1.186
13	0.504	0.013	96.788	1.640	0.514	0.012	98.117	1.484
14	0.514	0.013	98.134	1.650	0.510	0.013	97.614	1.629
15	0.513	0.015	97.937	1.866	0.507	0.016	97.237	1.998
16	0.505	0.012	96.986	1.516	0.511	0.013	97.686	1.621
17	0.506	0.009	97.129	1.074	0.509	0.013	97.416	1.592
18	0.521	0.019	98.960	2.450	0.516	0.016	98.404	2.009
19	0.510	0.009	97.578	1.168	0.505	0.016	96.950	2.003
20	0.513	0.013	98.009	1.575	0.505	0.016	97.021	1.992
21	0.505	0.012	96.932	1.540	0.508	0.020	97.291	2.482
22	0.513	0.010	97.919	1.207	0.509	0.015	97.416	1.845

TABLE 3.1: The results of the cylinder average heights and related droplet volumes. To estimate the droplet volumes (V), droplets were geometrically approximated as cylinders capped with hemispherical ends. The radius of both the cylindrical and hemispherical sections was assumed to be half the microchannel width (0.2 mm). The height of the cylindrical portion ($H_{cylinder}$) was determined by repeatedly measuring the length of the droplet in contact with the channel (7 measurements – H_{err} is the error related to these measurements). Based on the calculated volumes, the average droplet volume was determined to be 97.62 ± 0.30 nL at Metering Trap 1 and 97.68 ± 0.27 nL at Metering Trap 2.

Chapter 4

Summary

This dissertation presents a comprehensive quantitative and mechanistic analysis of nucleic acid hybridization in aqueous environments. It emphasizes how chemical composition and physical conditions influence the thermodynamic and kinetic parameters governing DNA association. Through systematic investigation of charged catalysts, ionic strength modulation, and macromolecular crowding, the work demonstrates that both the rate and equilibrium of hybridization can be precisely modulated by rationally designing the surrounding milieu. Eventually, the thesis demonstrates a semi-automated platform to speed up measurements of nucleic acid hybridization studies.

The introduction of positively charged catalysts – ranging from simple monomers to polymers and micelles – was shown to accelerate hybridization by several orders of magnitude relative to conventional ionic buffers. This enhancement is attributed to increased local concentrations of DNA at catalyst surfaces, where electrostatic attraction between the catalyst and DNA overcomes the mutual repulsion between negatively charged strands. The acceleration was most pronounced when the charge was concentrated on fewer catalyst particles, yielding higher local charge density. A physical model developed in this work quantitatively links catalyst charge magnitude and distribution to the observed rate enhancement. These findings establish that reaction rates can be tuned over multiple orders of magnitude by adjusting catalyst properties, with broad implications for molecular sensing, signal amplification, and the development of chemical logic systems.[113–116] For instance, rate enhancement mechanisms could be employed to detect specific

ionic species in solution or to amplify signals originating from highly dilute analytes.

Further, the equilibrium properties of DNA hybridization are shown to exhibit a non-monotonic response to increasing concentrations of molecular crowders. At moderate concentrations, depletion forces predominate, favoring duplex formation and leading to a substantial increase in the equilibrium constant. However, as the concentration of crowders increases further, crowding-induced destabilization becomes the dominant factor, impeding the association of DNA strands and reducing binding affinity by several orders of magnitude. Additionally, crowders bind ions from solution, decreasing electrostatic screening of reactants. This dualistic behavior is accurately captured and explained by the phenomenological model to provide a unified framework for understanding hybridization under crowded conditions. The simple, quadratic model predicts both the initial increase in K and the subsequent inhibition of DNA-DNA binding. As such, this model may serve as a practical tool for optimizing in vitro studies under crowded conditions.[109, 117] Future extensions may implement Debye–Hückel theory and the Asakura–Oosawa model to quantitatively describe the contributions of electrostatics, depletion interactions, and remaining crowding-induced destabilizing effects.

Finally, to address the throughput and efficiency limitations of FCS-based equilibrium studies, this thesis introduces a microfluidic-based platform that accelerates K measurements. By integrating sample preparation, dilution, mixing, and measurement within a single streamlined workflow, the system automates the most time-consuming experimental stages while maintaining the precision of the measurement. This platform leverages nanoliter-volume droplets, handled within a reusable droplet-on-demand and detection units, allowing for serial titration and real-time fluorescence-based analysis via MBA/FRET and FCS. As a result, the overall operator time required for a single K measurement is reduced by more than three hours in relation to the standard protocol. Beyond efficiency, the approach offers economic and environmental advantages: reagent consumption is decreased by 2000 times, and the need for disposable multiwell plates is eliminated, reducing material costs and laboratory waste. Importantly, this miniaturized system enhances measurement reliability and reproducibility by minimizing human

intervention and standardizing sample handling. The versatility of the platform allows for systematic variation of all solution components and studies of biomolecule interactions under diverse conditions. Though it is not a fully automated solution, the proposed platform is a crucial step towards closed-loop FCS-based measurements. By enabling high-throughput and low-volume quantitative analysis of molecular interactions, this platform may serve as a foundation for adaptive, feedback-controlled experiments in diagnostics, drug discovery, and systems biology.

Taken together, the results presented in this dissertation establish a comprehensive and predictive framework for understanding and controlling nucleic acid hybridization reactions, bridging the gap from manual measurements to semi-automated analysis. By elucidating the mechanisms by which charged catalysts, ionic composition, and macromolecular crowding govern both the kinetics and equilibria of DNA association, this work demonstrates how hybridization can be tuned over several orders of magnitude through rational manipulation of environmental conditions. The physical models developed herein enable quantitative predictions of nucleic acid systems. The introduction of a microfluidic-based platform further translates these insights into a tool that increases the efficiency of studies.

Bibliography

(1) Zhang, D. Y.; Chen, S. X.; Yin, P. *Nature chemistry* **2012**, *4*, 208–214.

(2) Mangla, P.; Vicentini, Q.; Biscans, A. *Cells* **2023**, *12*, 2253.

(3) Ratan, Z. A.; Zaman, S. B.; Mehta, V.; Haidere, M. F.; Runa, N. J.; Akter, N.; RATAN, Z. A. *Cureus* **2017**, *9*.

(4) Fu, Z.; Lu, Y.-C.; Lai, J. J. *Chonnam medical journal* **2019**, *55*, 86–98.

(5) Bumgarner, R. *Current protocols in molecular biology* **2013**, *101*, 22–1.

(6) Shalon, D.; Smith, S. J.; Brown, P. O. *Genome research* **1996**, *6*, 639–645.

(7) Salataj, E.; Spilianakis, C. G.; Chaumeil, J. *Frontiers in Immunology* **2023**, *14*, 1156077.

(8) Watts, J. K.; Corey, D. R. *The Journal of pathology* **2011**, *226*, 365.

(9) Wong, K. L.; Liu, J. *Biotechnology journal* **2021**, *16*, 2000338.

(10) Swenson, C. S.; Lackey, H. H.; Reece, E. J.; Harris, J. M.; Heemstra, J. M.; Peterson, E. M. *RSC Chemical Biology* **2021**, *2*, 1249–1256.

(11) Markarian, M. Z.; Schlenoff, J. B. *The Journal of Physical Chemistry B* **2010**, *114*, 10620–10627.

(12) Scott, S.; Shaheen, C.; McGuinness, B.; Metera, K.; Kouzine, F.; Levens, D.; Benham, C. J.; Leslie, S. *Nucleic acids research* **2019**, *47*, 6360–6368.

(13) Baltierra-Jasso, L. E.; Morten, M. J.; Laflör, L.; Quinn, S. D.; Magennis, S. W. *Journal of the American Chemical Society* **2015**, *137*, 16020–16023.

(14) Bielec, K.; Kowalski, A.; Bubak, G.; Witkowska Nery, E.; Hołyst, R. *The Journal of Physical Chemistry Letters* **2021**, *13*, 112–117.

(15) Kucharska, K.; Pilz, M.; Bielec, K.; Kalwarczyk, T.; Kuźma, P.; Hołyst, R. *Molecules* **2021**, *26*, 3748.

(16) Zhou, Y.; Bielec, K.; Pasitsuparoad, P.; Hołyst, R. *Analyst* **2020**, *145*, 6600–6606.

(17) Shen, Y.; Wu, S.-Y.; Rancic, V.; Aggarwal, A.; Qian, Y.; Miyashita, S.-I.; Ballanyi, K.; Campbell, R. E.; Dong, M. *Communications biology* **2019**, *2*, 18.

(18) Boersma, A. J.; Liu, B.; Poolman, B. *Biophysical Journal* **2015**, *108*, 114a.

(19) Liu, B.; Poolman, B.; Boersma, A. J. *ACS chemical biology* **2017**, *12*, 2510–2514.

(20) Chen, H.; Ding, F.; Zhou, Z.; He, X.; Shen, J. *Analyst* **2020**, *145*, 4283–4294.

(21) Bielec, K.; Bubak, G.; Kalwarczyk, T.; Holyst, R. *The Journal of Physical Chemistry B* **2020**, *124*, 1941–1948.

(22) Xue, C.; Greene, E. C. *Trends in Genetics* **2021**, *37*, 639–656.

(23) Liao, H.; Wu, J.; VanDusen, N. J.; Li, Y.; Zheng, Y. *Molecular Therapy Nucleic Acids* **2024**, *35*.

(24) Sumner, C. J.; Miller, T. M., et al. *The Journal of Clinical Investigation* **2024**, *134*.

(25) Gebert, L. F.; Rebhan, M. A.; Crivelli, S. E.; Denzler, R.; Stoffel, M.; Hall, J. *Nucleic acids research* **2014**, *42*, 609–621.

(26) Sett, A.; Das, S.; Bora, U. *Applied biochemistry and biotechnology* **2014**, *174*, 1073–1091.

(27) Gao, F.; Yin, J.; Chen, Y.; Guo, C.; Hu, H.; Su, J. *Frontiers in bioengineering and biotechnology* **2022**, *10*, 972933.

(28) Faria, M.; Wood, C.; Perrouault, L.; Nelson, J.; Winter, A.; White, M.; Helene, C.; Giovannangeli, C. *Proceedings of the National Academy of Sciences* **2000**, *97*, 3862–3867.

(29) Crooke, S. T.; Vickers, T. A.; Liang, X.-h. *Nucleic acids research* **2020**, *48*, 5235–5253.

(30) Roberts, T. C.; Langer, R.; Wood, M. J. *Nature reviews Drug discovery* **2020**, *19*, 673–694.

(31) Xie, N.; Zhang, L.; Gao, W.; Huang, C.; Huber, P. E.; Zhou, X.; Li, C.; Shen, G.; Zou, B. *Signal transduction and targeted therapy* **2020**, *5*, 227.

(32) Kirschning, A. *Angewandte Chemie International Edition* **2021**, *60*, 6242–6269.

(33) Huang, F. *Nucleic Acids Research* **2003**, *31*, e8–e8.

(34) Krall, J. B.; Nichols, P. J.; Henen, M. A.; Vicens, Q.; Vögeli, B. *Molecules* **2023**, *28*, 843.

(35) Obara, P.; Wolski, P.; Pańczyk, T. *Molecules* **2024**, *29*, 4683.

(36) Kilburn, D.; Roh, J. H.; Guo, L.; Briber, R. M.; Woodson, S. A. *Journal of the American Chemical Society* **2010**, *132*, 8690–8696.

(37) Denesyuk, N. A.; Thirumalai, D. *Biophysical reviews* **2013**, *5*, 225–232.

(38) Miyoshi, D.; Sugimoto, N. *Biochimie* **2008**, *90*, 1040–1051.

(39) Ellis, R. J.; Minton, A. P. *Nature* **2003**, *425*, 27–28.

(40) Zimmerman, S. B.; Trach, S. O. *Journal of molecular biology* **1991**, *222*, 599–620.

(41) Zhou, H.-X.; Rivas, G.; Minton, A. P. *Annu. Rev. Biophys.* **2008**, *37*, 375–397.

(42) Ellis, R. J. *Trends in biochemical sciences* **2001**, *26*, 597–604.

(43) Danielsson, J.; Mu, X.; Lang, L.; Wang, H.; Binolfi, A.; Theillet, F.-X.; Bekei, B.; Logan, D. T.; Selenko, P.; Wennerström, H., et al. *Proceedings of the National Academy of Sciences* **2015**, *112*, 12402–12407.

(44) Gnutt, D.; Gao, M.; Brylski, O.; Heyden, M.; Ebbinghaus, S. *Angewandte Chemie International Edition* **2015**, *54*, 2548–2551.

(45) Sukenik, S.; Sapir, L.; Harries, D. *Current opinion in colloid & interface science* **2013**, *18*, 495–501.

(46) Lim, W. K.; Denton, A. R. *The Journal of chemical physics* **2016**, *144*.

(47) Zosel, F.; Soranno, A.; Buholzer, K. J.; Nettels, D.; Schuler, B. *Proceedings of the National Academy of Sciences* **2020**, *117*, 13480–13489.

(48) Gudimchuk, N. B.; McIntosh, J. R. *Nature reviews Molecular cell biology* **2021**, *22*, 777–795.

(49) Rivas, G.; Minton, A. P. *Trends in biochemical sciences* **2016**, *41*, 970–981.

(50) Minton, A. P. *Journal of biological chemistry* **2001**, *276*, 10577–10580.

(51) Cheung, M. S.; Klimov, D.; Thirumalai, D. *Proceedings of the National Academy of Sciences* **2005**, *102*, 4753–4758.

(52) Patel, A.; Malinovska, L.; Saha, S.; Wang, J.; Alberti, S.; Krishnan, Y.; Hyman, A. A. *Science* **2017**, *356*, 753–756.

(53) Record Jr, M. T.; Ha, J.-H.; Fisher, M. A. In *Methods in enzymology*; Elsevier: 1991; Vol. 208, pp 291–343.

(54) Zhou, H.-X. *Archives of biochemistry and biophysics* **2008**, *469*, 76–82.

(55) Fok, S. W.; Gresham, R. C.; Ryan, W.; Osipov, B.; Bahney, C.; Leach, J. K. *Frontiers in Bioengineering and Biotechnology* **2023**, *11*, 1091157.

(56) Kasahara, K.; Re, S.; Nawrocki, G.; Oshima, H.; Mishima-Tsumagari, C.; Miyata-Yabuki, Y.; Kukimoto-Niino, M.; Yu, I.; Shirouzu, M.; Feig, M., et al. *Nature communications* **2021**, *12*, 4099.

(57) Atkins, P. W.; De Paula, J.; Keeler, J., *Atkins' physical chemistry*; Oxford university press: 2023.

(58) Laidler, K. J.; Keith, J., et al., *Chemical kinetics*; McGraw-Hill New York: 1965; Vol. 2.

(59) SantaLucia Jr, J.; Hicks, D. *Annu. Rev. Biophys. Biomol. Struct.* **2004**, *33*, 415–440.

(60) Lakowicz, J. *University of Maryland School of Medicine Baltimore* **2006**, *132*.

(61) Perez-Howard, G. M.; Weil, P. A.; Beechem, J. M. *Biochemistry* **1995**, *34*, 8005–8017.

(62) House, J. E., *Principles of chemical kinetics*; Academic press: 2007.

(63) Schmidt, L. D. et al., *The engineering of chemical reactions*; Oxford University Press New York: 2005.

(64) Jablonski, A. *Nature* **1933**, *131*, 839–840.

(65) Franck, J.; Dymond, E. *Transactions of the Faraday Society* **1926**, *21*, 536–542.

(66) Stokes, G. G. *Philosophical transactions of the Royal Society of London* **1852**, 463–562.

(67) Han, C.; Wang, R.; Wang, K.; Xu, H.; Sui, M.; Li, J.; Xu, K. *Biosensors and Bioelectronics* **2016**, *83*, 229–236.

(68) Klymchenko, A. S. *Accounts of chemical research* **2017**, *50*, 366–375.

(69) Bajar, B. T.; Wang, E. S.; Zhang, S.; Lin, M. Z.; Chu, J. *Sensors* **2016**, *16*, 1488.

(70) Danylchuk, D. I.; Moon, S.; Xu, K.; Klymchenko, A. S. *Angewandte Chemie* **2019**, *131*, 15062–15066.

(71) Lavis, L. D.; Raines, R. T. *ACS chemical biology* **2008**, *3*, 142–155.

(72) Sasaki, A. *Biophysical Reviews* **2022**, *14*, 33–39.

(73) Weber, M.; Huisken, J. *Frontiers in Cell and Developmental Biology* **2021**, *9*, 739015.

(74) Giloh, H.; Sedat, J. W. *Science* **1982**, *217*, 1252–1255.

(75) Patterson, G. H.; Piston, D. W. *Biophysical journal* **2000**, *78*, 2159–2162.

(76) Baibakov, M.; Patra, S.; Claude, J.-B.; Moreau, A.; Lumeau, J.; Wenger, J. *ACS nano* **2019**, *13*, 8469–8480.

(77) Squires, T. M.; Quake, S. R. *Reviews of modern physics* **2005**, *77*, 977–1026.

(78) Whitesides, G. M. *nature* **2006**, *442*, 368–373.

(79) Sackmann, E. K.; Fulton, A. L.; Beebe, D. J. *Nature* **2014**, *507*, 181–189.

(80) Reyes, D. R.; Iossifidis, D.; Auroux, P.-A.; Manz, A. *Analytical chemistry* **2002**, *74*, 2623–2636.

(81) Ottesen, E. A.; Hong, J. W.; Quake, S. R.; Leadbetter, J. R. *science* **2006**, *314*, 1464–1467.

(82) Stroock, A. D.; Dertinger, S. K.; Ajdari, A.; Mezic, I.; Stone, H. A.; Whitesides, G. M. *Science* **2002**, *295*, 647–651.

(83) Beebe, D. J.; Mensing, G. A.; Walker, G. M. *Annual review of biomedical engineering* **2002**, *4*, 261–286.

(84) Madou, M. J., *Manufacturing techniques for microfabrication and nanotechnology*; CRC press: 2011.

(85) Bhattacharjee, N.; Urrios, A.; Kang, S.; Folch, A. *Lab on a Chip* **2016**, *16*, 1720–1742.

(86) Martinez, A. W.; Phillips, S. T.; Whitesides, G. M.; Carrilho, E. Diagnostics for the developing world: microfluidic paper-based analytical devices, 2010.

(87) Macosko, E. Z.; Basu, A.; Satija, R.; Nemesh, J.; Shekhar, K.; Goldman, M.; Tirosh, I.; Bialas, A. R.; Kamitaki, N.; Martersteck, E. M., et al. *Cell* **2015**, *161*, 1202–1214.

(88) Huh, D.; Hamilton, G. A.; Ingber, D. E. *Trends in cell biology* **2011**, *21*, 745–754.

(89) Bhatia, S. N.; Ingber, D. E. *Nature biotechnology* **2014**, *32*, 760–772.

(90) Zhang, Y.; Nguyen, N.-T. *Lab on a Chip* **2017**, *17*, 994–1008.

(91) Bielec, K.; Sozanski, K.; Seynen, M.; Dziekan, Z.; Ten Wolde, P. R.; Holyst, R. *Physical Chemistry Chemical Physics* **2019**, *21*, 10798–10807.

(92) Friend, J.; Yeo, L. *Biomicrofluidics* **2010**, *4*.

(93) Liubysh, O.; Vlasiuk, A.; Perepelytsya, S. *arXiv preprint arXiv:1503.05334* **2015**.

(94) Peterson, A. W.; Heaton, R. J.; Georgiadis, R. M. *Nucleic acids research* **2001**, *29*, 5163–5168.

(95) Halford, S. E.; Marko, J. F. *Nucleic acids research* **2004**, *32*, 3040–3052.

(96) Blainey, P. C.; Luo, G.; Kou, S.; Mangel, W. F.; Verdine, G. L.; Bagchi, B.; Xie, X. S. *Nature structural & molecular biology* **2009**, *16*, 1224–1229.

(97) Morga, M.; Batys, P.; Kosior, D.; Bonarek, P.; Adamczyk, Z. *International journal of environmental research and public health* **2022**, *19*, 3588.

(98) DeRouchey, J.; Hoover, B.; Rau, D. C. *Biochemistry* **2013**, *52*, 3000–3009.

(99) Rafati, A. A.; Gharibi, H.; Rezaie-Sameti, M. *Journal of molecular liquids* **2004**, *111*, 109–116.

(100) Karumbamkandathil, A.; Ghosh, S.; Anand, U.; Saha, P.; Mukherjee, M.; Mukherjee, S. *Chemical Physics Letters* **2014**, *593*, 115–121.

(101) Mehta, S.; Chaudhary, S.; Bhasin, K. *Journal of colloid and interface science* **2008**, *321*, 426–433.

(102) Husale, S.; Grange, W.; Karle, M.; Bürgi, S.; Hegner, M. *Nucleic Acids Research* **2008**, *36*, 1443–1449.

(103) Grueso, E.; Sanchez, F. *The Journal of Physical Chemistry B* **2008**, *112*, 698–702.

(104) Kowalski, A.; Bielec, K.; Bubak, G.; Żuk, P. J.; Czajkowski, M.; Sashuk, V.; Huck, W. T.; Antosiewicz, J. M.; Holyst, R. *Nature Communications* **2022**, *13*, 6451.

(105) Smith, A. M.; Lee, A. A.; Perkin, S. *The journal of physical chemistry letters* **2016**, *7*, 2157–2163.

(106) Zhang, C.; Tian, F.-J.; Zuo, H.-W.; Qiu, Q.-Y.; Zhang, J.-H.; Wei, W.; Tan, Z.-J.; Zhang, Y.; Wu, W.-Q.; Dai, L., et al. *Nature Communications* **2025**, *16*, 113.

(107) Savitzky, A.; Golay, M. J. *Analytical chemistry* **1964**, *36*, 1627–1639.

(108) Jaiswal, A. K.; Srivastava, R.; Pandey, P.; Bandyopadhyay, P. *PloS one* **2018**, *13*, e0206359.

(109) Nakano, S.-i.; Miyoshi, D.; Sugimoto, N. *Chemical reviews* **2014**, *114*, 2733–2758.

(110) Asakura, S.; Oosawa, F. *The Journal of chemical physics* **1954**, *22*, 1255–1256.

(111) Korczyk, P. M.; Derzsi, L.; Jakieła, S.; Garstecki, P. *Lab on a Chip* **2013**, *13*, 4096–4102.

(112) Zaremba, D.; Blonski, S.; Korczyk, P. M. *Chemical Engineering Journal* **2022**, *430*, 132935.

(113) Wang, J.; Raito, H.; Shimada, N.; Maruyama, A. *Small* **2023**, *19*, 2304091.

(114) Jiao, Y.; Shang, Y.; Li, N.; Ding, B. *Iscience* **2022**, *25*.

(115) Li, Z.; Zhou, X.; Li, L.; Liu, S.; Wang, C.; Li, L.; Yu, C.; Su, X. *Analytical Chemistry* **2018**, *90*, 6804–6810.

(116) Hanpanich, O.; Oyanagi, T.; Shimada, N.; Maruyama, A. *Biomaterials* **2019**, *225*, 119535.

(117) McGuffee, S. R.; Elcock, A. H. *PLoS computational biology* **2010**, *6*, e1000694.